A SYSTEM LEVEL SIMULATION STUDY OF WiMAX

A THESIS

SUBMITTED TO THE DEPARTMENT OF ELECTRICAL AND

ELECTRONICS ENGINEERING

AND THE INSTITUTE OF ENGINEERING AND SCIENCES

OF BILKENT UNIVERSITY

IN PARTIAL FULFILLMENT OF THE REQUIREMENTS

FOR THE DEGREE OF

MASTER OF SCIENCE

By

Yüksel Ozan Başçiftçi

July 2010

I certify that I have read this thesis and that in my opinion it is fully adequate, in scope and in quality, as a thesis for the degree of Master of Science.

Prof. Dr. Erdal Arıkan(Supervisor)

I certify that I have read this thesis and that in my opinion it is fully adequate, in scope and in quality, as a thesis for the degree of Master of Science.

Prof. Dr. Mehmet Şafak

I certify that I have read this thesis and that in my opinion it is fully adequate, in scope and in quality, as a thesis for the degree of Master of Science.

Assoc. Prof. Dr. Ezhan Karaşan

Approved for the Institute of Engineering and Sciences:

Prof. Dr. Levent Onural
Director of Institute of Engineering and Sciences

ABSTRACT

A SYSTEM LEVEL SIMULATION STUDY OF WiMAX

Yüksel Ozan Başçiftçi
M.S. in Electrical and Electronics Engineering
Supervisor: Prof. Dr. Erdal Arıkan
July 2010

In this thesis, we implement a WiMAX system level simulator compliant with the evaluation methodology document published by the IEEE 802.16m Task Group. We study the PHY abstraction of polar codes and integrate polar codes into the simulator. We compare the system level performances of polar code and convolutional turbo code (CTC) and observe that CTC outperforms polar code.

On the simulator, we study the downlink (DL) performance of WiMAX under various configurations such as scheduling methods, subchannelization methods, and frequency reuse models. We study there types of scheduling methods, namely round robin (RR) scheduling, proportional fair (PF) scheduling, and maximum sum rate (MSR) scheduling. We observe that MSR scheduling has the best throughput performance but does not support the users far from the base station. We study three frequency reuse models, namely $1 \times 3 \times 1$, $1 \times 3 \times 3$, and $3 \times 3 \times 1$. We observe that $1 \times 3 \times 1$ reuse model has the best throughput performance and maximum spectral efficiency is obtained in $1 \times 3 \times 3$ reuse model. We study two subchannelization methods, namely PUSC and band AMC. We observe that in low mobility cases, band AMC outperforms PUSC and in high mobility cases, PUSC is better than band AMC.

Keywords: WiMAX, system level simulation, PHY abstraction, polar codes, IEEE 802.16m

ÖZET

SİSTEM SEVİYESİNDE WiMAX SİMULASYONU ÇALIŞMASI

Yüksel Ozan Başçiftçi
Elektrik ve Elektronik Mühendisliği Bölümü Yüksek Lisans
Tez Yöneticisi: Prof. Dr. Erdal Arıkan
Temmuz 2010

Bu tezde, sistem seviyesinde WiMAX benzeticisi gerçekleştirdik. Benzetici, IEEE 802.16 Görev Grubu m tarafından yayınlanan yöntem dokümanı ile uyumludur. Tezde, kutuplaşma kodlarının fiziksel katman soyutlanması üzerine çalıştık ve kutuplaşma kodlarını benzeticiye entegre ettik. Kutuplaşma kodları ile evrişimsel turbo kodların sistem seviyesindeki başarımlarını karşılaştırdık ve evrişimsel turbo kodların daha iyi bir başarıma sahip olduğunu gözlemledik.

Benzetici üzerinde WiMAX'in aşağı bağlantı başarımını farklı yapılanışlarda inceledik. Round robin (RR), proportional fair (PF) ve maximum sum ratio (MSR) olmak üzere, üç farklı kaynak atama yöntemi üzerinde çalıştık. MSR kaynak atama yönteminin veri hızı bakımından en iyi başarıma sahip olduğunu fakat baz istasyonundan uzaktaki kullanıcılara servis veremediğini gözlemledik. $1 \times 3 \times 3$, $3 \times 3 \times 1$ ve $1 \times 3 \times 1$ olmak üzere, üç adet frekans planlama metodu üzerine çalıştık. En yüksek veri hızını $1 \times 3 \times 1$ metodunda ve en yüksek spektral verimliliği $1 \times 3 \times 3$ metodunda gözlemledik. Bant AMC ve PUSC alt kanal ayrıştırma yöntemleri üzerine çalıştık. Yüksek hızlarda bant AMC'nin PUSC'dan daha iyi başarıma sahip olduğunu, düşük hızlarda ise PUSC'un başarımının daha iyi olduğunu gözlemledik.

Anahtar Kelimeler: WiMAX, sistem seviyesinde simulasyon, fiziksel katman soyutlaması, kutuplaşma kodları, IEEE 802.16m

ACKNOWLEDGMENTS

I would like to thank my advisor Prof. Erdal Arıkan for his guidance and support throughout my thesis research. I would also like to thank Professors Mehmet Şafak and Ezhan Karaşan for being my thesis defense committee.

I would like to thank my family, my father Muhsin, my mother Gülderen, my brother Halis, and my sister Gizem for their endless support throughout my life.

I would also like to thank Ahmet Serdar Tan for writing the initial version of the system level simulator.

Finally, I would like to thank TÜBİTAK 107E216 Project, FP7 215167 WiMAGIC Project, and FP7 216715 Newcom++ Project for their financial support.

Contents

List of Figures

List of Tables

Abbreviations

AMC Adaptive Modulation and Coding

AWGN Additive white Gaussian noise

BLER Block Error Rate

BS Base Station

CDF Cumulative Distribution Function

CQI Channel Quality Indicator

CTC Convolutional Turbo Code

DL Downlink

EMD 802.16m Evaluation Methodology Document

ESM Effective SINR Mapping

EESM Exponential Effective SINR Mapping

FFT Fast Fourier Transform

FUSC Full Usage of Subcarriers

ITU International Telecommunication Union

RB Resource Block

MCS Modulation and Coding Scheme

MIC Mean Instantaneous Capacity

MIMO Multiple-Input Multiple-Output

MMIB Mean Mutual Information per Bit

MS Mobile Station

MSR Maximum Sum Rate

OFDM Orthogonal Frequency Division Multiplexing

OFDMA Orthogonal Frequency Division Multiple Access

PER Packet Error Rate

PHY Physical Layer

PUSC Partial Usage of Subcarriers

RBIR Received Bit Mutual Information Rate

RR Round Robin

SNR Signal to Noise Ratio

SINR Signal to Interference-plus-Noise Ratio

UL Uplink

WiMAX Worldwide Interoperability for Microwave Access

To my mother Gülderen Başçiftçi...

Chapter 1

Introduction

Worldwide Interoperability for Microwave Access (WiMAX) is a recent technology that offers mobile broadband wireless access to multimedia and Internet applications [1]. IEEE 802.16e standard [2] specifies medium access control layer (MAC) and physical layer of WiMAX. Figure 1.1 shows a simple WiMAX network.

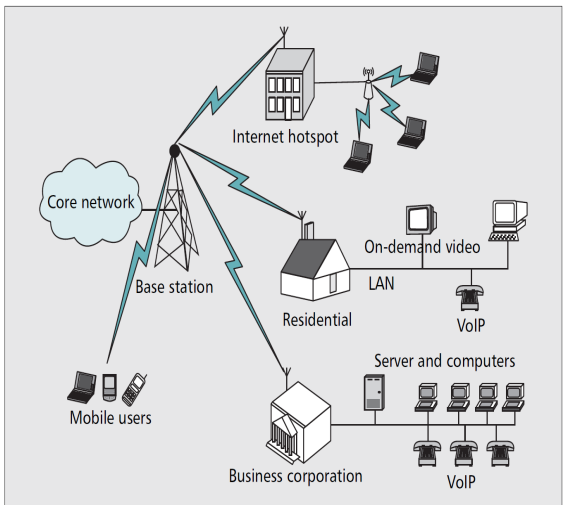

Figure 1.1: WiMAX scenario [3].

Computer simulations are vital for the analysis of telecommunication networks such as WiMAX because they are too complex to be handled by analytical

methods. Computer simulations of telecommunication networks are separated into two categories: link level simulations and system level simulations. Link level simulations study the transmission between a single base station (BS) and a mobile station (MS). A methodology for a link level simulation of broadband wireless systems such as WiMAX is provided in [4, Chapter 11]. The performance of the downlink (DL) and uplink (UL) of WiMAX is studied with link level simulations in [5]. System level simulations are used to evaluate the system level performance of telecommunication networks, consisting of multiple BSs and MSs.

In telecommunications networks, BSs and MSs using the frequency band interfere to each other. Figure 1.2 shows a sample interference scenario for DL transmission. From Figure 1.2, we can observe that the signals of the interfering BSs and MSs mix with the signal of the serving BS at the given MS. To evaluate the performance of wireless network exactly, we should model the interference as in the real world. Since link level simulations contain a single BS and MS,

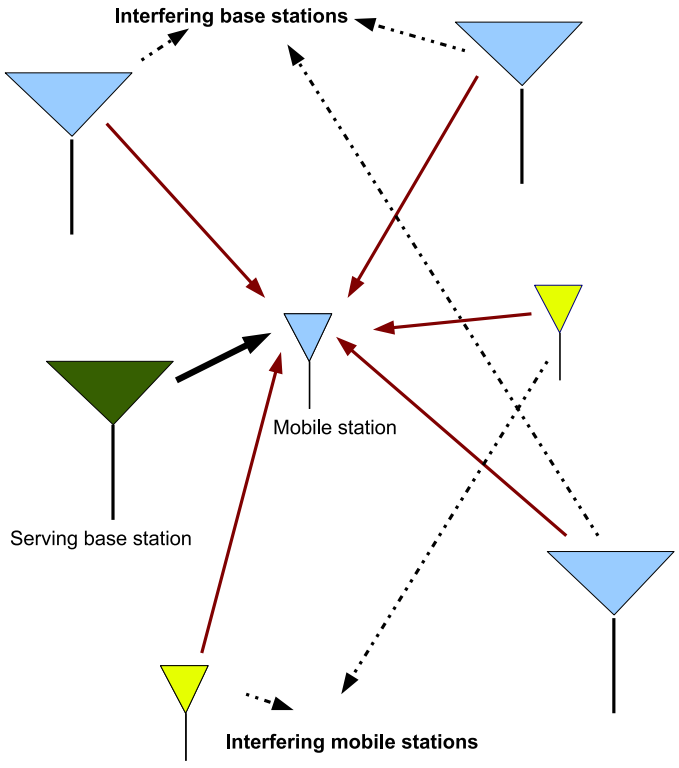

Figure 1.2: A sample DL interference scenario.

the effect of an interference is modeled by random variable that has a specific probability distribution. However, with the help of system level simulations, we can model the interference accurately because system level simulations employ multiple BSs and MSs and each link between them is simulated.

The IEEE 802.16m Task Group has published an evaluation methodology document (EMD) [6] for researchers who have interest in the system level simulation of IEEE 802.16e based networks. The system level performance of WiMAX is discussed in [7], [8], and [9]. WiMAX is compared with 3G technologies namely, 3GPP and 3GPP2 with the help of system level simulations in [10] and [11].

1.1 The Problem

In a system level simulation, the number of links in the telecommunication network can reach up to thousands depending on the number of the BSs and MSs. Simulating the physical layer communication of each link has huge computational complexity.

The solution of that problem is to develop a model which predicts the performance of the physical layer, comprising the elements shown in Figure 1.3 under a given channel model. This model is called physical layer (PHY) abstraction.

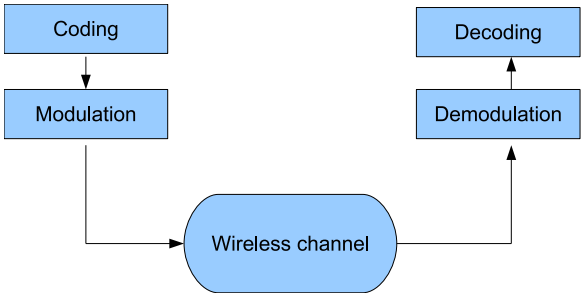

Figure 1.3: Illustration of physical layer.

A physical layer abstraction method is an interface between system level and link level simulations. The explanation of how the physical layers are abstracted is as follows. In the link level simulations, the physical layer simulations are done under AWGN channel for different coding and modulation schemes. These simulations output curves reflecting the performance of the physical layers. In the system level simulations, the wireless channels including the effects of interference and fading are generated and the performance of the physical layers under the generated wireless channels are estimated by using the performance curves from the link level simulations.

1.2 Thesis Contributions

In this thesis, we implemented a WiMAX system level simulator based on the methodology given in [6]. We studied the PHY abstraction of polar codes. Polar codes, recently introduced by Arıkan in [12] are the first low-complexity codes that theoretically achieve symmetric capacity of binary-input discrete memoryless channels. We integrated polar codes into the simulator and performed system level performance comparison simulations with the convolutional turbo code configurations (CTC) defined in [13, p.1038].

On the system level simulator, we evaluated the DL performance of WiMAX under various configurations. We studied the effect of mobility. We implemented three frequency reuse models, namely $1 \times 3 \times 1$, $1 \times 3 \times 3$, $3 \times 3 \times 1$ and compared the performance of these frequency reuse models. We studied three scheduling methods, namely round robin scheduling, proportional fair scheduling, and maximum sum rate scheduling. Lastly, we investigated the performance of two subchannelization methods, namely partial usage of subcarriers (PUSC) and band AMC.

1.3 Organization of the Thesis

The rest of the thesis is organized as follows. In Chapter 2, we introduce essential concepts of WiMAX, including WiMAX frame structure, adaptive modulation and coding, scheduling, hybrid automatic repeat-request, and data mapping. We study these concepts in the next chapters. In Chapter 3, we introduce the wireless channel model and frequency reuse models used in the system level simulations. Then, we explain the PHY abstraction methodology in detail. Lastly, we provide the system level simulation methodology. In Chapter 4, simulation results are presented and discussed. In Chapter 5, we summarize our conclusions and provide research directions for future.

Chapter 2

WiMAX System Description

In this chapter, we explain the features of WiMAX that are implemented in the system level simulator. Firstly, we present the WiMAX frame structure and then, we introduce the scheduling, adaptive modulation and coding (AMC), and hybrid automatic repeat request (HARQ) concepts. At the end of this chapter, we explain how the data of a user is mapped to a WiMAX frame.

2.1 WiMAX Frame Structure

WiMAX physical layer is based on Orthogonal Frequency-Division Multiplexing (OFDM). OFDM is a multicarrier modulation scheme implemented by fast Fourier transform (FFT) algorithm. In OFDM, a high rate serial data stream is divided into a parallel set of low rate substreams which are simultaneously transmitted. These parallel streams are recombined at the receiver into a single high rate stream. Each substream is modulated on a separate subcarrier.

The number of subcarriers in an OFDM symbol is equal to the FFT size. WiMAX has three types of subcarriers, namely data subcarriers, pilot subcarriers, and null subcarriers. Data subcarriers are used for data transmission. Pilot

subcarriers are used for channel estimation. Training symbols are sent on the pilot subcarriers and response of the channel on these subcarriers is evaluated. Null subcarriers include the DC subcarrier and guard subcarriers. No data is sent on the null subcarriers. Figure 2.1 displays the frequency domain representation of an OFDM symbol. As seen in the figure, no power is allocated to the null subcarriers.

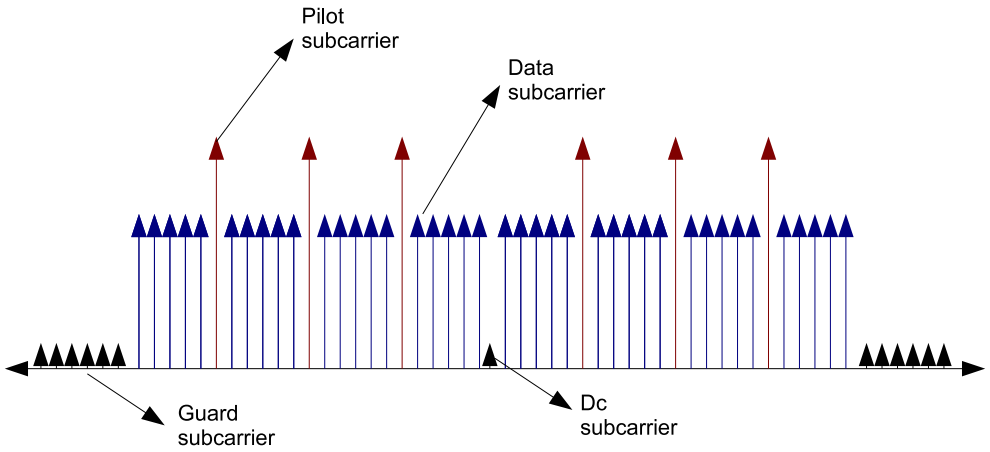

Figure 2.1: Frequency domain representation of an OFDM symbol.

2.1.1 Subchannelization

In WiMAX terminology, a subchannel means a group of subcarriers together by specific methods as defined in the standard. Subchannels represent the minimum granularity for allocation of frequency resources. Subchannels are allocated to users by BSs. This type of multi access technique is called Orthogonal Frequency-Division Multiplexing Access (OFDMA).

Subchannelization method determines how the subcarriers are grouped into subchannels. WiMAX supports several subchannelization schemes, namely DL-PUSC, UL-PUSC, FUSC, and band AMC. Detailed explanation of these subchannelization schemes can be found in [13, Section 8.4.6]. In this thesis, we will concentrate only on DL-PUSC and band AMC.

In band AMC, each subchannel is assigned a contiguous set of subcarriers. In DL-PUSC, subcarriers are divided into clusters. Each cluster contains 14 adjacent subcarriers over two OFDM symbols. There are 12 data subcarriers and two pilot subcarriers in each symbol of a cluster. The clusters are renumbered using a pseudo-random numbering scheme. Next, pilot subcarriers in the clusters are taken away. Then, the clusters are divided into six groups. A subchannel is formed by combining two clusters from the same group. There are 24 data subcarriers and four pilot subcarriers in each symbol of a subchannel. Table 2.1 specifies the DL-PUSC parameters for different FFT sizes.

FFT size	128	512	1024	2048
Subcarriers per cluster	14	14	14	14
Number of subchannels	3	15	30	60
Data subcarriers used	72	360	720	1440
Pilot subcarriers	12	60	120	240
Left-guard subcarriers	22	46	92	184
Right-guard subcarriers	21	45	91	183

Table 2.1: Parameters of DL-PUSC subchannelization.

2.1.2 Frame Structure

A slot is the minimum time-frequency data resource unit in WiMAX. Each slot spans several OFDM symbols over a single subchannel. The size of a slot depends on the subchannelization scheme that is used. Table 2.2 provides the slot sizes for each subchannelization scheme. The set of adjacent slots assigned to a user

Subchannelization scheme	Slot size (subcarrier $\times$ OFDM symbol)
DL-PUSC	24×2
UL-PUSC	16×3
FUSC	48×1
Band AMC	8×6, 16×3, 24×2

Table 2.2: Slot sizes for subchannelization schemes DL-PUSC, UL-PUSC, FUSC, and band AMC.

is called a data region or burst for that user. A data region is transmitted with a same burst profile. The burst profile of a data region represents the selected modulation format, code rate, and type of forward error correcting (FEC) code for that data region. Table 8.4 in [4] provides the uplink and downlink burst profiles supported in IEEE 802.16e standard [13].

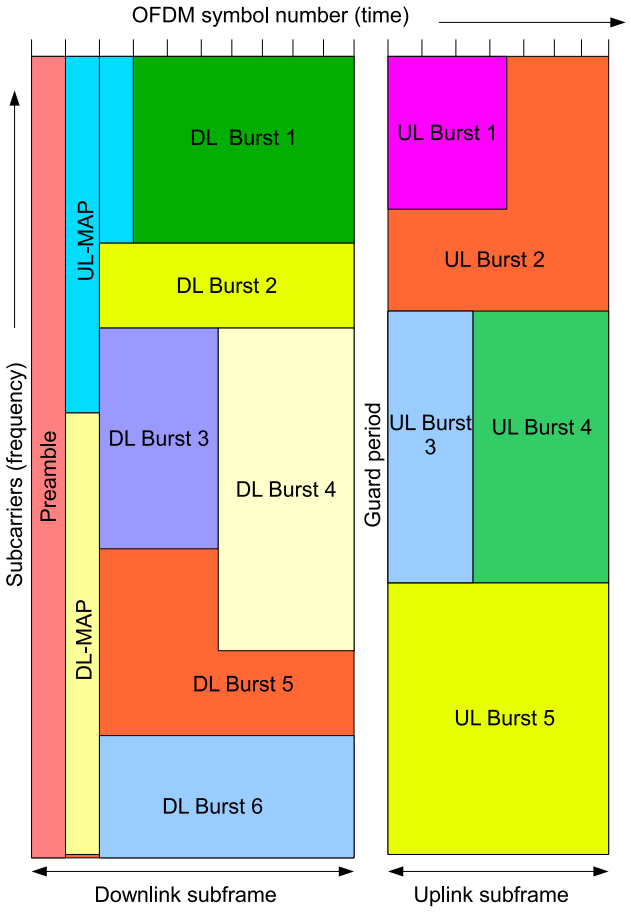

Figure 2.2: A sample WiMAX frame structure.

Figure 2.2 displays the structure of a WiMAX frame. Time division duplexing (TDD) scheme is employed in the WiMAX frame. The frame is divided into two subframes: DL subframe and UL subframe. There is a guard period between the subframes. The frame begins with a preamble, DL-MAP message, and UL-MAP message. These messages are followed by the data regions of users.

Preamble is used for time and frequency synchronization. DL-MAP and UL-MAP messages indicate where the data regions of users are located on WiMAX

frame and which modulation and coding scheme (MCS) is selected throughout these regions.

A WiMAX frame is composed of 48 OFDM symbols. Each OFDM symbol has duration of 102.82 μs and the duration of the guard period between the uplink and downlink subframes is 0.1057 ms. The total duration of a WiMAX frame is 5.043 ms.

WiMAX supports high peak data rates. For example; assume that the data region of a WiMAX DL subframe includes 24 OFDM symbols and each OFDM symbol contains 720 data subcarriers. If all DL data is transmitted with 5/6 rate error correcting code with 64-QAM modulation, peak data rate for the downlink is $\frac{720\times24\times5}{4.9373\times10^{-3}} = 17.5$Mbps.

2.2 Adaptive Modulation and Coding

In time-varying and multipath channels, received power changes in both time and frequency domain. AMC is used to adapt the data transmission rate according to the channel conditions. Data transmission rate is adjusted by changing the order of modulation schemes and the rate of error correcting codes. For example, in good channel conditions, high rate FEC codes and high order modulation schemes are selected to support high data rate transmission.

In WiMAX, support for QPSK, 16QAM and 64QAM are mandatory in the DL. In the UL, support for 64QAM is optional. Convolutional Code (CC), CTC, and repetition code at different code rates are supported. In the UL, support for code rate 5/6 is optional. Block Turbo Code and Low Density Parity Check Code (LDPC) are supported as optional features in WiMAX. Table 2.3 displays the supported codes and modulations in WiMAX.

	DL	UL
Modulation	QPSK, 16-QAM, 64-QAM	QPSK, 16-QAM, 64-QAM
Coding	CC, Rates:1/2, 2/3, 3/4, 5/6 CTC, Rates:1/2, 2/3, 3/4, 5/6 Rep. codes, Rates: 1/2, 1/4, 1/6	CC, Rates:1/2, 2/3, 3/4, 5/6 CTC, Rates:1/2, 2/3, 3/4, 5/6 Rep. codes, Rates: 1/2, 1/4, 1/6

Table 2.3: Supported codes and modulations in WiMAX.

In WiMAX, each MS feeds back channel quality indicator (CQI) to its serving BS in order to describe the DL channel condition. For the uplink, BS can estimate the channel condition according to the received signal quality. Based on the uplink and downlink channel conditions of MSs, BS assigns a MCS to each burst. This assignment is done in accordance to the AMC algorithm employed by BSs. We will provide our AMC algorithm in Section 3.4.3.

2.3 Scheduling

In WiMAX, the aim of scheduling is to distribute the data regions among the MSs based on QoS requirements and channel conditions. IEEE 802.16e standard [13] does not include a specific scheduling algorithm. In Chapter 3.4.3, we will provide three scheduling methods, namely proportional fair scheduling, maximum sum rate scheduling, and round robin scheduling.

2.4 HARQ

Hybrid automatic repeat-request (HARQ) is an error-correction technique that improves the reliability of packet transmission by combining medium access layer and PHY layer FEC coding [14]. In WiMAX, when a receiver fails to decode a received packet correctly, the packet is retransmitted in accordance to the HARQ

method. IEEE 802.16e standard [13] supports two types of HARQ methods, namely Chase combining and incremental redundancy.

In the Chase combining method, retransmitted data blocks and the original data block are encoded with the same coding scheme. A current retransmitted data block is combined with previous transmissions and fed into FEC decoder. In the incremental redundancy method, each retransmitted data block is encoded differently. In each retransmission, additional redundant information is transmitted; therefore, coding rate decreases in each retransmission. Detailed information about these two methods is provided in [4, Section 8.2].

2.5 Data Mapping

When a user is assigned to a particular burst, the data of that user is mapped to a burst slot by slot. A slot is the minimum data resource in WiMAX frame and supports only a small FEC block. Therefore, slots are concatenated in order to support large FEC blocks.

A concatenation rule determines how to split data into FEC blocks. IEEE 802.16e standard [13] proposes concatenation rules for each type of FEC code used in WiMAX. In this thesis, we will concentrate only on the concatenation rule specified for CTC. Table 2.4, taken from [13, Section 8.4.9.2], specifies the concatenation rule. Table 2.6 displays the code block lengths of CTC used in the slot concatenation algorithm and also displays the number of slots concatenated for each code block.

Description of the parameters in Table 2.4 is as follows. n is the number of slots allocated to a scheduled user. j is the maximum number of the slots that can be concatenated for each MCS as shown in Table 2.5. k is floor(n/j) and m is n mod (j).

Number	**Slots concatenated**
$n \leq j$ $n \neq 7$	1 block of n slots
$n \leq j \quad n = 7$	1 block of 4 slots 1 block of 3 slots

$n > 7$	If (n mod $j = 0$)
	k blocks of j slots
	else
	k - 1 blocks of j slots
	1 block of L_{b1} slots
	1 block of L_{b2} slots
	where
	$L_{b2} = \text{floor}((m + j)/2)$
	$L_{b1} = \text{ceil}((m + j)/2)$
	If ($L_{b1} = 7$) or ($L_{b2} = 7$)
	$L_{b1} = L_{b1} + 1; L_{b2} = L_{b2} - 1;$

Table 2.4: Slot concatenation rule.

MCS	**j**
CTC-QPSK-1/2	10
CTC-QPSK-3/4	6
CTC-16-QAM-1/2	5
CTC-16-QAM-3/4	3
CTC-64-QAM-1/2	3
CTC-64-QAM-2/3	2
CTC-64-QAM-3/4	2
CTC-64-QAM-5/6	2

Table 2.5: Maximum number of slots concatenated for each MCS.

We will give an example to clarify the data mapping. Assume that each burst contains 24 slots and the supported MCS of the user who is assigned to a particular burst is CTC-QPSK-1/2. Then, the parameters in Table 2.4 are as follows: n = 24, j = 10, k = 2, and m = 2.

The mapping of the data is as follows. Burst is partitioned into 1 block of 10 slots, 1 block of 8 slots, and 1 block of 6 slots in accordance to the concatenation algorithm. Then, we choose the appropriate code profiles of QPSK-1/2 that fit into each slot block. From Table 2.6, we can see that profiles 9, 7, and 6 fit into

Profile No.	MCS	Data block size (bytes)	Encoded block size (bytes)	Number of concatenated slots
1	QPSK-1/2	6	12	1
2	QPSK-1/2	12	24	2
3	QPSK-1/2	18	36	3
4	QPSK-1/2	24	48	4
5	QPSK-1/2	30	60	5
6	QPSK-1/2	36	72	6
7	QPSK-1/2	48	96	8
8	QPSK-1/2	54	108	9
9	QPSK-1/2	60	120	10
10	QPSK-3/4	9	12	1
11	QPSK-3/4	18	24	2
12	QPSK-3/4	27	36	3
13	QPSK-3/4	36	48	4
14	QPSK-3/4	45	60	5
15	QPSK-3/4	54	72	6
16	16-QAM-1/2	12	24	1
17	16-QAM-1/2	24	48	2
18	16-QAM-1/2	36	72	3
19	16-QAM-1/2	48	96	4
20	16-QAM-1/2	60	120	5
21	16-QAM-3/4	18	24	1
22	16-QAM-3/4	36	48	2
23	16-QAM-3/4	54	72	3
24	64-QAM-1/2	18	36	1
25	64-QAM-1/2	36	72	2
26	64-QAM-1/2	54	108	3
27	64-QAM-2/3	24	36	1
28	64-QAM-2/3	48	72	2
29	64-QAM-3/4	27	36	1
30	64-QAM-3/4	54	72	2
31	64-QAM-5/6	30	36	1
32	64-QAM-5/6	60	72	2

Table 2.6: Data block sizes used in convolutional turbo coding.

10-slotted, 8-slotted, and 6-slotted blocks respectively. The data sent through the burst is $60 + 48 + 36 = 144$ bytes.

Chapter 3

System Level Simulation

In this chapter, firstly, we will provide the wireless channel model, the frequency reuse models, and the PHY abstraction models. Then, we will describe the system level simulation methodology that is compliant with the EMD [6]. We will also explain in this chapter the specific algorithm implementations that were used in the system level simulations.

3.1 Wireless Channel Model

In this section, we will explain the wireless channel model in terms of two sub-models, which are large scale fading model and small scale fading model. The description here is a summary of the full description given in [6, Section 3.2.9].

3.1.1 Large Scale Fading Model

Large scale fading model predicts the behavior of the channel averaged over distances larger than the wavelength of the signal. Large scale fading model includes the effects of path loss, antenna gain, and shadowing.

3.1.1.1 Path Loss

Path loss describes the attenuation of the signal power mainly as a function of distance between the transmitter and the receiver. Due to the complex nature of propagation channels, empirical path loss models are used instead of the analytical models.

We are using the empirical path loss model described in [6, Section 3.2.3]. The model is as follows:

$$\mathrm{PL_{dB}} = 40(1 - 4 \times 10^{-3}\mathrm{h_{BS}}) \log_{10}(\mathrm{R}) - 18 \log_{10}(\mathrm{h_{BS}}) + 21 \log_{10}(\mathrm{f}) + 80, \quad (3.1)$$

where $\mathrm{PL_{dB}}$ is the path loss in decibels (dB), R is the distance from the transmitter to the receiver in kilometers, f is the carrier frequency in MHz and $\mathrm{h_{BS}}$ is the BS antenna height above rooftop in meters. For example, when $\mathrm{h_{BS}}$ is fixed at 15 meters and f is taken 2.5 GHz, the path loss model reduces to

$$\mathrm{PL_{dB}} = 128.1 + 37.6 \log_{10}(\mathrm{R}). \quad (3.2)$$

3.1.1.2 Antenna Gain

BSs include 120 degree spaced directional antennas in our simulations. The radiation pattern for the BS antennas in the horizontal plane is expressed by

$$G(\theta) = -\min\left(12\left(\frac{\theta}{\theta_{3\mathrm{dB}}}, \mathrm{A_m}\right)\right), \quad \text{where} -180 \leq \theta \leq 180. \quad (3.3)$$

In the above expressions, $G(\theta)$ is the gain in the direction of horizontal angle θ, $\mathrm{A_m}$ is the minimum gain ($\mathrm{A_m} = -20$ dB), and $\theta_{3\mathrm{dB}}$ is the 3 dB beam width ($\theta_{3\mathrm{dB}} = 70^o$). BS antennas are assumed to be omni-directional in the vertical plane and MS antenna is assumed to be omni-directional in both planes.

3.1.1.3 Shadowing

Shadowing describes the random variation at received signal power due to blockage from objects. Shadowing is modeled as having a log-normal distribution[1]. Shadowing experienced by the users who are close to each other is correlated.

The correlation is modeled with the help of a shadowing factor grid as shown in Figure 3.1. Shadowing factor experienced on the link between MS x and BS l can be expressed as

$$\begin{aligned} \mathrm{SF_{dB,l}(x)} = \sqrt{1-\frac{\mathrm{x_{pos}}}{\mathrm{D_{cor}}}}\left[\mathrm{S_{0,l}}\sqrt{\frac{\mathrm{y_{pos}}}{\mathrm{D_{cor}}}}+\mathrm{S_{3,l}}\sqrt{1-\frac{\mathrm{y_{pos}}}{\mathrm{D_{cor}}}}\right]+ \\ \left[\mathrm{S_{1,l}}\sqrt{\frac{\mathrm{y_{pos}}}{\mathrm{D_{cor}}}}+S_{2,l}\sqrt{1-\frac{\mathrm{y_{pos}}}{\mathrm{D_{cor}}}}\right]\sqrt{\frac{\mathrm{x_{pos}}}{\mathrm{D_{cor}}}}, \end{aligned} \tag{3.4}$$

where

$\mathrm{D_{cor}}$: De-correlation distance and distance between the closest nodes,

$\mathrm{S_{n,l}}$: Shadowing factor experienced on the link between node n and BS l,

$\mathrm{S_{0,l}}$,$\mathrm{S_{1,l}}$,$\mathrm{S_{2,l}}$,$\mathrm{S_{3,l}}$: Shadowing factors experienced on the link between the closest nodes to MS x and BS l,

$\mathrm{x_{pos}}$, $\mathrm{y_{pos}}$: Coordinates of user x on the specified square of the grid. $\mathrm{D_{cor}}$ is equal to 50 meters in the simulations. We will skip the calculation of $\mathrm{S_{n,l}}$'s which is explained in [6, Section 3.2.4].

3.1.2 Small Scale Fading Model

Small scale fading model predicts the variability in signal over distances on the orders of the signal wavelength. The model includes the multipath effect and the Doppler effect. The multi path effect is modeled by a tapped delay line model

$$h(l,t) = \sum_{l=1}^{\mathrm{N}} \alpha(l,t)\delta(\tau-\tau_l) \tag{3.5}$$

[1]Log-normal distribution is a probability distribution of a random variable whose logarithm is a normal random variable.

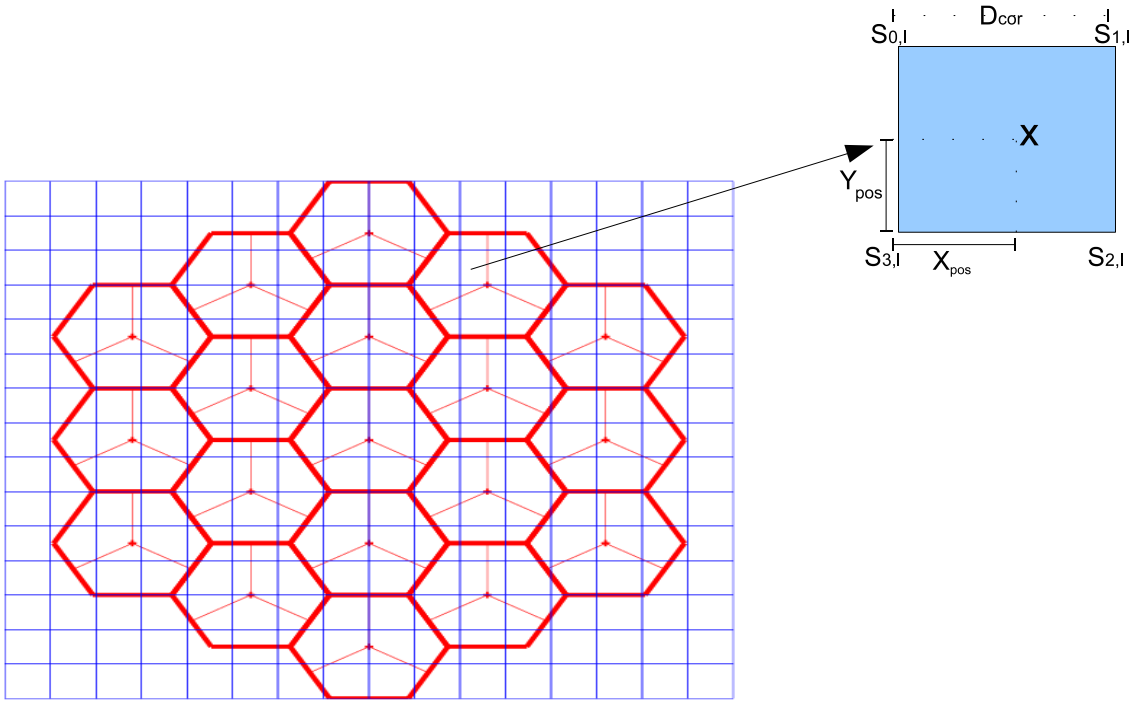

Figure 3.1: Grid structure on the hexagonal cells [6].

where $h(l,t)$ is the impulse response of l^{th} path at time t, $\alpha(l,\tau_l)$ is the complex amplitude of the l^{th} path at time t, τ_l is the time delay of the l^{th} path and N is the number of resolvable paths.

ITU modified pedestrian B and ITU modified vehicular A channel models are used for the multi path effect. Table 3.1 specifies the power delay profiles of these models. Doppler effect is modeled by Clarke's uniform scattering environment model which is explained in [15, Chapter 3].

Path Index	**Modified Pedestrian B**		**Modified Vehicular A**	
	Power(dB)	Delay(ns)	Power(dB)	Delay(ns)
1	-1.175	0	-3.1031	0
2	0	40	-0.4166	50
3	-0.1729	70	0	90
4	-0.2113	120	-1.0065	130
5	-0.2661	210	-1.4083	270
6	-0.3963	250	-1.4436	300
7	-4.32	290	-1.5443	390
8	-1.1608	350	-4.0437	420
9	-10.4232	780	-16.6369	670
10	-5.7198	830	-14.3955	750
11	-3.4798	880	-4.9259	770
12	-4.1745	920	-16.516	800
13	-10.1101	1200	-9.2222	1040
14	-5.646	1250	-11.9058	1060
15	-10.0817	1310	-10.1378	1070
16	-9.4109	1350	-14.1861	1190
17	-13.9434	2290	-16.9901	1670
18	-9.1845	2350	-13.2515	1710
19	-5.5766	2380	-14.8881	1820
20	-7.6455	2400	-30.348	1840
21	-38.1923	3700	-19.5257	2480
22	-22.3097	3730	-19.0286	2500
23	-26.0472	3760	-38.1504	2540
24	-21.6155	3870	-20.7436	2620

Table 3.1: Power delay profiles of ITU modified pedestrian B and ITU modified vehicular A channels.

3.2 Frequency Reuse Models

In this thesis, we consider the deployment of WiMAX as a cellular network. Each cell in the network has a hexagonal structure and has a single BS in the center. Each directional antenna located in a BS is called a sector.

Frequency reuse refers to allocating the same spectrum band to different sector or cells. We will use three frequency reuse models in our simulations. A frequency reuse model is denoted by a triple $N_c \times N_s \times N_f$ [16], where N_c is the ratio of the entire bandwidth to the bandwidth allocated for each cell, N_s is the

number of sectors per cell and N_f is the ratio of the bandwidth allocated for a cell to the bandwidth allocated for a sector.

Figure 3.2 shows the network deployment for the frequency reuse patterns that will be studied in this thesis. In $1 \times 3 \times 1$ reuse mode, each sector in the network is assigned the whole spectrum, f1. In $1 \times 3 \times 3$ reuse mode, each cell in the network is also assigned whole spectrum but the whole spectrum is divided into three segments, namely f1, f2, and f3, and each sector in a particular cell is assigned only one of the segments. In $3 \times 3 \times 1$ reuse mode, the whole spectrum band is divided into three segments, namely f1, f2, and f3 and each cell is assigned only one of the segments. Sectors in a particular cell are assigned the same segment.

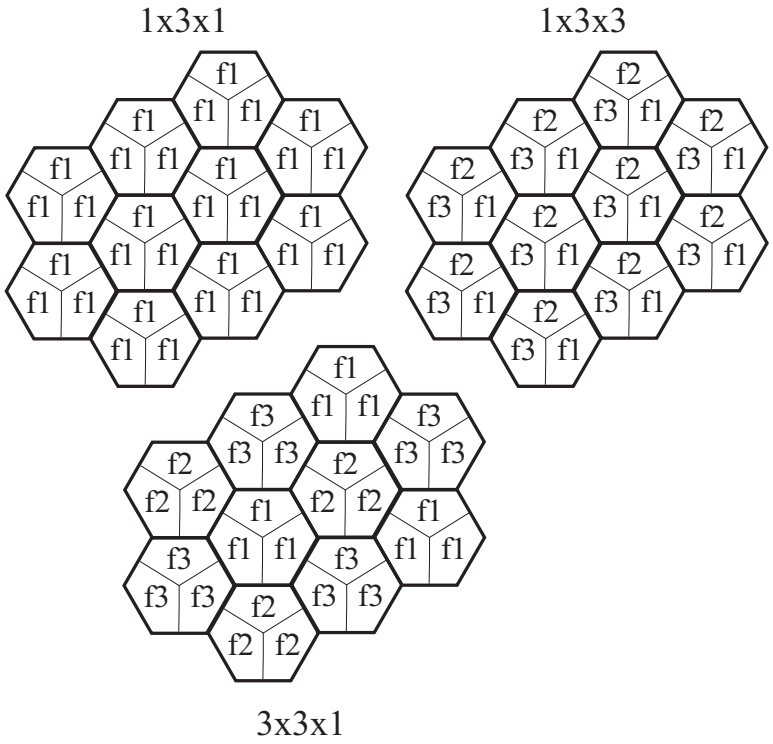

Figure 3.2: Frequency reuse patterns used in the simulations.

3.3 Physical Layer Abstraction Methodology

Physical layer (PHY) abstraction aims to predict instantaneous link level performance. In this section, we will explain the methodology of the PHY abstraction.

3.3.1 Post-Processing SINR Computation per Tone

First step of the PHY abstraction methodology is to compute the post- processing SINR of the received signal. The received signal on the desired MS is [6]

$$\mathbf{y}[\mathrm{n}] = \sqrt{\mathrm{P}_0^{\mathrm{r}}}\mathbf{H}_0[\mathrm{n}]\mathbf{x}_0[\mathrm{n}] + \sum_{k=1}^{\mathrm{K}} \sqrt{\mathrm{P}_{\mathrm{k}}^{\mathrm{r}}}\mathbf{H}_{\mathrm{k}}[\mathrm{n}]\mathbf{x}_{\mathrm{k}}[\mathrm{n}] + \mathrm{w}[\mathrm{n}], \tag{3.6}$$

where

y[n] is the $\mathrm{P} \times 1$ vector of received symbols, $\mathrm{x_k}[\mathrm{n}]$ is $\mathrm{Q} \times 1$ vector of symbols transmitted from the $\mathrm{k^{th}}$ sector on the subcarrier n, $\mathrm{H_k}[\mathrm{n}]$ is $\mathrm{P} \times \mathrm{Q}$ channel matrix on the link between the $\mathrm{k^{th}}$ sector and the desired MS, K is the number of interferers, w[n] is the additive white Gaussian noise (AWGN) with variance σ_n^2, P and Q are the number of receive and transmit antennas respectively, sector with index 0 is the serving sector. $\mathrm{P_k^r}$ is the average power received from the $\mathrm{k^{th}}$ sector,

$$\mathrm{P_k^r} = \frac{(\mathrm{P_k^t})(\mathrm{SF_k})(\mathrm{G_k})}{\mathrm{PL_k}}, \tag{3.7}$$

where $\mathrm{P_k^t}$ is the transmitted power per subcarrier from the $\mathrm{k^{th}}$ sector, $\mathrm{SF_k}, \mathrm{G_k},$ and $\mathrm{PL_k}$ are the shadowing factor, the antenna gain and the path loss for the link between the $\mathrm{k^{th}}$ sector and the MS of interest respectively.

In our simulations, we study single input single output (SISO), single input multiple output (SIMO), and multiple input multiple output (MIMO) systems. In each system, received signal is processed by a different receiver algorithm and SINR is computed from the processed signal. We will only give the SINR computation in SISO systems. The computation of the post-processing SINR on

SIMO and MIMO systems can be found in [6, pp.81–85].

In SISO, assuming a matched filter receiver, the post-processed signal z[n] is

$$\mathrm{z[n]} = \mathrm{H_0[n]^* y[n]}, \tag{3.8}$$

and the post-processing SINR after the matched filter is

$$\mathrm{SINR[n]} = \frac{\mathrm{P_0^r |H_0[n]|^2}}{\sum_{\mathrm{k=1}}^{\mathrm{K}} \mathrm{P_k^r |H_k[n]|^2} + \sigma_n^2}. \tag{3.9}$$

3.3.2 ESM PHY Abstraction

Due to the frequency and time selectivity of a wireless channel, subcarriers that are used to transmit a FEC code experience different SINR values. The aim of the PHY abstraction is to predict the block error rate (BLER) of a FEC code when the SINR values on the used subcarriers and the chosen MCS of the FEC code are given.

With the effective SINR mapping (ESM), SINR values on the subcarriers used to transmit a FEC block is compressed to a single value, called effective SINR. Effective SINR ($\mathrm{SINR_{eff}}$) is mapped onto "AWGN signal to noise ratio (SNR) vs BLER" curves to find the BLER of the FEC block. This process is called ESM PHY abstraction.

The ESM PHY abstraction methodology is as follows:

1. The instantaneous SINR values on the used subcarriers are calculated.
2. These SINR values are mapped to a single value, $\mathrm{SINR_{eff}}$ with mapping function f.
$$\mathrm{SINR_{eff}} = \mathrm{f}(\mathrm{SINR}_1, \mathrm{SINR}_2, \cdots, \mathrm{SINR}_N) \tag{3.10}$$
3. According to the MCS of the FEC block, proper AWGN curve is selected and the BLER value that corresponds to $\mathrm{SINR_{eff}}$ is found on the curve.

The AWGN SNR vs BLER curves are generated with link level simulations and stored in look up tables. Therefore, predicting the BLER for a particular FEC block is a very fast process in system level simulations.

The methodology for EESM PHY abstraction can be seen in Figure 3.3. It can be observed that PHY abstraction maps the inputs from a system level simulation to a single performance metric such as a BLER.

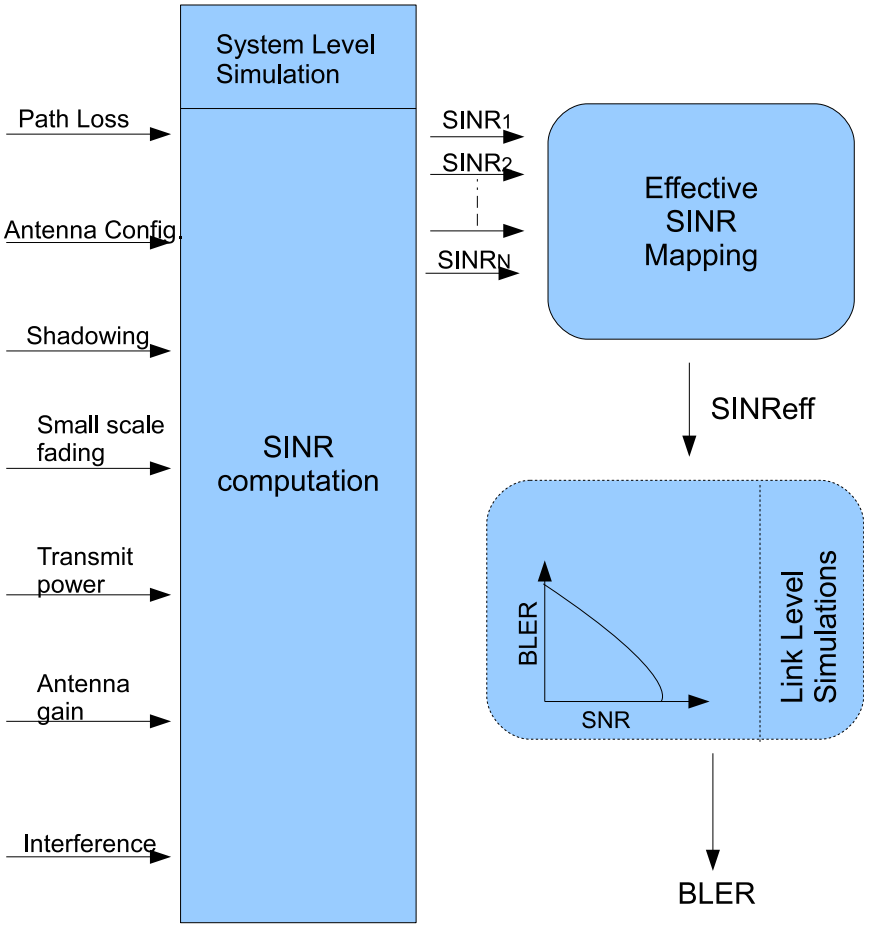

Figure 3.3: Illustration of EESM PHY abstraction.

There are three ESM PHY abstraction methods in the literature; mutual information effective SINR mapping (MIESM), exponential effective SINR mapping (EESM), and mean instantaneous capacity (MIC).

In ESM PHY abstraction, the structure of the mapping function is as follows,

$$\mathrm{SINR_{eff}} = \mathrm{g}^{-1}\left(\frac{1}{\mathrm{N}}\sum_{\mathrm{i}=1}^{\mathrm{N}}\mathrm{g}\left(\mathrm{SINR}[\mathrm{n_i}]\right)\right), \tag{3.11}$$

where N is the number of the used subcarriers [6], $\mathrm{SINR}[\mathrm{n_i}]$ is the SINR value in the $\mathrm{n_i^{th}}$ subcarrier, $\{\mathrm{n_1}, \mathrm{n_2}, \cdots, \mathrm{n_N}\}$ are the indexes of the subcarriers that are used and g is an invertible function.

In the MIESM method, the mutual informations of the used subcarriers are calculated. Then, the mutual informatio are averaged over the used subcarriers. To find $\mathrm{SINR_{eff}}$, the averaged value is mapped onto "modulation constrained capacity vs SNR curve", seen in Figure 3.4, with matched modulation.

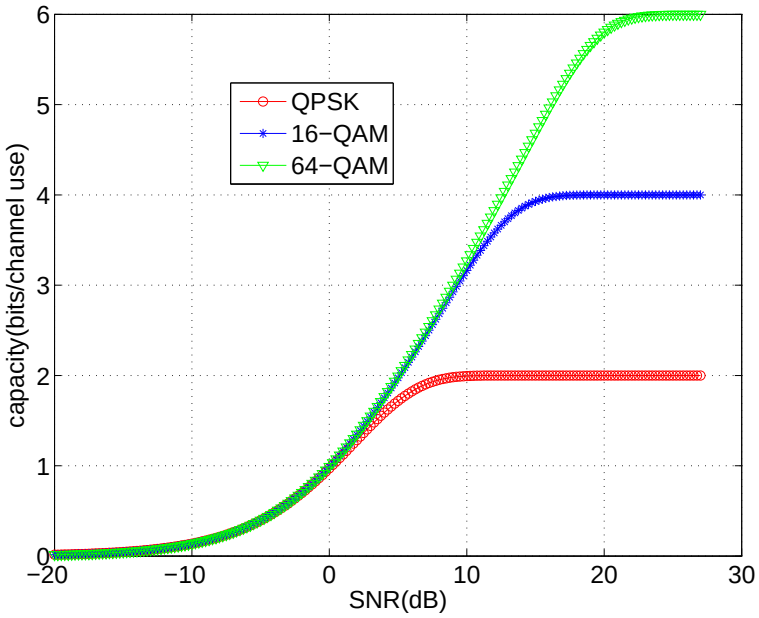

Figure 3.4: Constrained capacity of different modulation schemes [6].

There are two MIESM methods which differ only in the way mutual information is calculated. These methods are received bit mutual information rate (RBIR) ESM, and mean mutual information per bit (MMIB) ESM.

In the RBIR method, the mutual information of each subcarrier is described as a symbol level mutual information. Symbol level mutual information is the constrained capacity with related SNR and modulation scheme. In MMIB, each

symbol channel is divided into bit channels and bit level mutual information is calculated for each bit channel. Mutual information of each subcarrier is described as the sum of bit level mutual informations. The exact formulation of the MIESM methods are given in [6, Section 4.3].

In the EESM method, $\mathrm{SINR_{eff}}$ is computed as

$$\mathrm{SINR_{eff}} = -\beta \ln\left(\frac{1}{\mathrm{N}}\sum_{\mathrm{i}=1}^{\mathrm{N}} \exp\left(\frac{\mathrm{SINR}[\mathrm{n_i}]}{\beta}\right)\right), \tag{3.12}$$

where β is the adjustment value that depends on MCS and FEC block length [6]. Proper values of β can be found in [17, Appendix C.2]. It can be observed that here $\mathrm{g(x)} = \exp(\frac{\mathrm{x}}{\beta})$.

In the MIC method, $\mathrm{SINR_{eff}}$ is calculated using the relation in [17, Appendix C.3],

$$\mathrm{SINR_{eff}} = 2^{\left(\frac{1}{\mathrm{N}}\sum_{\mathrm{i}=1}^{\mathrm{N}} \log_2(\mathrm{SINR}[\mathrm{n_i}]+1)\right)}, \tag{3.13}$$

It can be observed that here $\mathrm{g(x)} = \log_2(\mathrm{x}+1)$. MIC method is used in the CQI feedback calculations.

In the simulations, we use Chase combining HARQ method. The PHY abstraction methodology for the Chase combining HARQ method that is described in [6, Section 4.6.2] is as follows. For each retransmission of the same FEC block, we obtain a vector of SINR values on the used subcarriers. We sum these vectors and obtain a single SINR vector. This vector of SINR values is compressed to a single SINR value with the ESM PHY abstraction methods explained above. For the FEC block in the retransmitted packet, $\mathrm{SINR_{eff}}$ can be calculated as

$$\mathrm{SINR_{eff}} = \mathrm{g}^{-1}\left(\frac{1}{\mathrm{N}}\sum_{\mathrm{i}=1}^{\mathrm{N}} \mathrm{g}\left(\sum_{\mathrm{r}=1}^{\mathrm{R}} \mathrm{SINR_r}[\mathrm{n_i}]\right)\right), \tag{3.14}$$

where R is the number of the transmission of the FEC block, N is the number of the used subcarriers [6], $\mathrm{SINR_r}[\mathrm{n_i}]$ is the SINR value in the $\mathrm{n_i^{th}}$ subcarrier for the $\mathrm{r^{th}}$ transmission and $\{\mathrm{n_1}, \mathrm{n_2}, \cdots \mathrm{n_N}\}$ are the indexes of the subcarriers used.

When the BLER of each FEC block in the packet is predicted, packet error rate (PER) is estimated in the following way

$$\mathrm{PER} = 1 - \prod_{\mathrm{k}=1}^{\mathrm{K}} (1 - \mathrm{BLER_k}), \tag{3.15}$$

where K is the number of the FEC blocks in the packet and $\mathrm{BLER_k}$ is the $\mathrm{k^{th}}$ FEC block in the packet.

3.4 Simulation Methodology

In this section, we will introduce the parts of the system level simulation which are configuration, initialization, simulation, and analysis.

OFDMA parameters and systems parameters that are the same in each simulation scenario are given in Table 3.2 and Table 3.3.

Parameters	**Value**
Bandwidth	10 MHz
Sampling frequency	11.2 MHz
FFT size	1024
Ratio of DL subframe duration to frame duration	1/2
Subcarrier spacing	10.94 kHz
OFDM symbol duration	102.86 us
Null subcarriers	184
Pilot subcarriers	120
Data subcarriers	720
Frame duration	5 ms
Number of OFDM symbols in frame	48
Number of OFDM symbols in DL subframe	29
Number of OFDM symbols allocated to preamble, DL-MAP and UL-MAP messages	5
Number of OFDM symbols allocated to DL data regions	24
Number of data subcarriers allocated to subchannel	24
Slot size	1 subchannel × 2 OFDM symbol

Table 3.2: OFDMA parameters used in the simulations.

Parameter	Value
Number of clusters	7
Number of cells per cluster	19
Number of sectors per cell	3
Number of sectors per cluster	57
Carrier frequency	2.5 GHz
BS to BS distance	1.5 km
Minimum MS to BS distance	35m
MS noise figure	7 dB
BS transmit power per sector/subcarrier	46 dBm
De-correlation distance for shadowing	50 m
Log normal shadowing standard deviation	8 dB
CQI feedback delay	3 frames
Maximum number of HARQ retransmissions	3 frames
Minimum HARQ retransmission delay	2 frames
Number of strong interferers, I_{strong}	8
Target BLER for AMC algorithm	0.01

Table 3.3: System parameters used in the simulations.

3.4.1 Configuration

In the configuration part, a simulation scenario is determined by the parameters given in Table 3.4.

Parameter	Value
Traffic	Full buffer
Scheduling method	PF, MSR, RR
Coding scheme	CTC, polar code
PHY abstraction method	EESM, MMIB, RBIR
Number of RBs per frame	5, 10, 15, 30
Antenna configuration	SISO, SIMO, MIMO
Subchannelization	PUSC, AMC
Number of MSs per sector N_{sec}	5, 10, 20, 30
Speed	3 km/h, 30 km/h, 120 km/h, mix
Frequency reuse pattern	1x3x1, 1x3x3, 3x3x1

Table 3.4: Input parameters used in the simulations.

If the velocity input is "mix", %60 of MSs have 3 km/h speed, %30 of MSs have 30 km/h speed, and %10 of MSs have 120 km/h speed. If the velocity input is not "mix", then all MSs are assigned the same speed as specified.

In MIMO configuration, there are 2 antennas at both receiving and transmitting sites, whereas in SIMO, there are 2 antennas at receiver site. MIMO configuration employs Alamouti scheme [18].

In addition to the parameters given in Table 3.4, *simulation time* and *drop number* are also specified in the configuration phase. Simulation time, T_{sim}, indicates the duration of simulation scenario. We repeat the simulation of each scenario with different seeds to get reliable results. Drop number, N_{drop}, indicates how many times the same scenario will be simulated.

3.4.2 Initialization

In the initialization part, cellular structure, which is given in Figure 3.5, is created. From Figure 3.5, it can be observed that there are 7 clusters and each of the clusters includes 19 cells. We only analyze the MSs served by the cells of central cluster. The outer clusters are modeled for accurate results. If the outer cells are missing, the co-channel interference[2] experienced by the MSs at the edge of central cluster will be modeled inaccurately.

Look-up tables including BLER vs SNR curves for given coding schemes are loaded.

Subcarriers are distributed to the sectors according to the frequency reuse pattern. Assigned subcarriers to the sectors are permuted with the selected subchannelization scheme.

[2]Co-channel interference is the interference between the MS and the sector using the same spectrum band

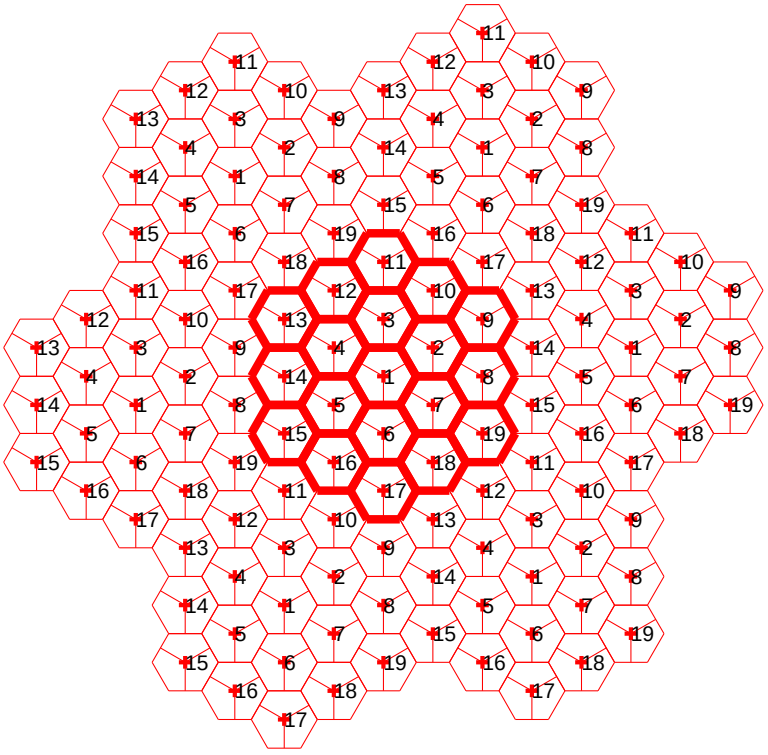

Figure 3.5: Cellular deployment with wrap around implementation.

3.4.3 Simulation

The simulation part is the most computationally heavy part of the system level simulation and includes 3 main blocks, namely "local initialization", "DL transmission", and "metric computation". These blocks can be seen in Figure 3.6.

3.4.3.1 Local Initialization

MSs are randomly dropped to the central cluster. Dropping stops when the number of MSs that each sector serves reaches N_{sec}. MSs are served by the sectors from which they receive the maximum average power. Eq. 3.7 shows the calculation of average received power.

In Eq. 3.7, the term $\frac{(SF_k)(G_k)}{PL_k}$ is referred to *link gain* on the link between the MS of interest and sector k. We assume MSs do not move during the simulation

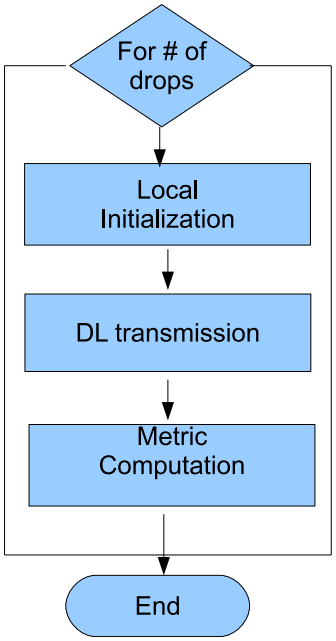

Figure 3.6: Illustration of the simulation part.

so the link gains do not change. We calculate the link gains for all links in the network and store them. They are used for the SINR computation and for determining the strong interferers to MSs.

The speed of each MS is determined according to the input configuration. MSs which have 3 km/h speed are assigned ITU modified pedestrian B channel model and MSs which have 30 km/h and 120 km/h speeds are assigned ITU modified vehicular A model. The assigned speeds are used only to model the Doppler effect.

3.4.3.2 DL Transmission

The structure of the DL transmission block is shown in Figure 3.7. The process shown in Figure 3.7 is repeated for each WiMAX frame. Figure 3.8 displays the downlink WiMAX frame structure that is used in the simulations. The frame is composed of P resource blocks (RB). The meaning of a RB is the same with burst or data region that are explained in Section 2.1.2. Each RB spans the

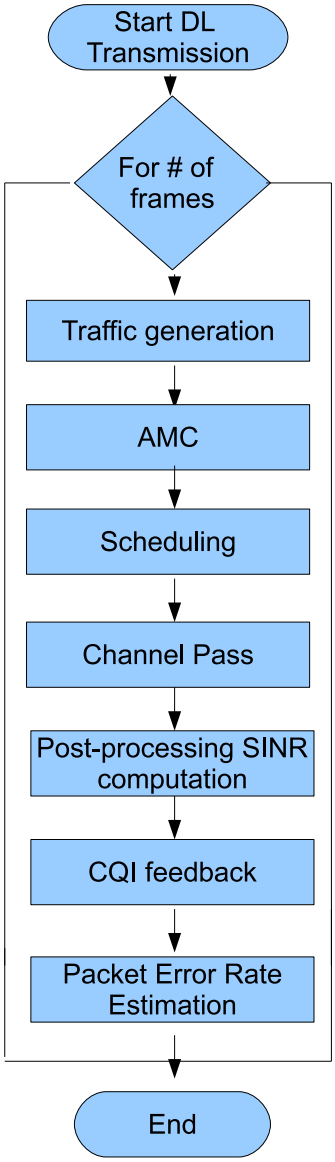

Figure 3.7: Illustration of the DL transmission.

entire frame in time domain over an integer number of subchannels. All RBs are rectangular and have the same size.

In our simulations, we assume that there is perfect time and frequency synchronization. Moreover, we assume each user knows the boundaries of its data region and its selected MCSs throughout this data region perfectly. Therefore, we do not use the functionality of preamble, DL-MAP, and UL-MAP messages but we reserve first few symbols of the frame to these messages as seen in Figure 3.8.

Explanation of the subblocks shown in Figure 3.7 are as follows.

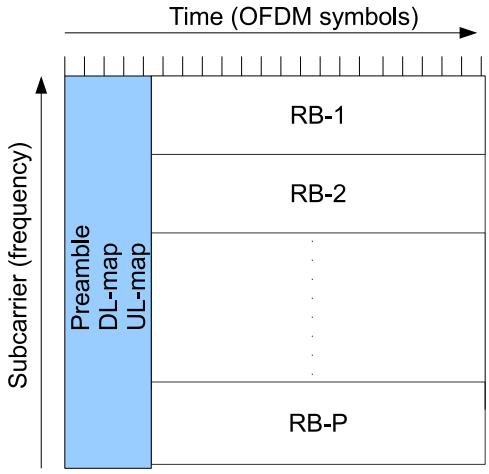

Figure 3.8: WiMAX downlink subframe.

Traffic generation subblock : In the simulations, full buffer traffic is assigned to all users. When a user is assigned to a particular RB, that user always has enough data to fill the RB and entire data sent on the RB is referred to as a packet.

AMC subblock : The supported MCS of each MS for each RB is determined in the AMC subblock. Table 3.5 displays the MCSs used in the simulations and also specifies the maximum spectral efficiencies (C^i_{max}) of each MCS. Figure 3.9 shows the performance of these MCSs for convolutional turbo coding in terms of spectral efficiency (C^i) vs SNR under AWGN channel. The spectral efficiency of the i^{th} MCS in the SNR value x, $C^i(x)$, is derived using the relation on [4, p.69], namely

$$C^i(x) = (1 - BLER_i(x)) \times C^i_{max}, \quad \text{where} \quad C^i_{max} = \log_2(M) \times r. \tag{3.16}$$

In the above expressions, $BLER_i(x)$ is the BLER of the i^{th} MCS in SNR value x. M and r are the modulation order and rate for the i^{th} MCS respectively.

The AMC algorithm used in the simulations is as follows,

$$MCS_{u,r} = \arg \max_{i:BLER_i \leq \text{target BLER}} C^i(CQI_{u,r}), \tag{3.17}$$

i	MCS	$C^i_{\max}$(bps/Hz)
1	QPSK-1/2	1
2	QPSK-3/4	1.5
3	16QAM-1/2	2
4	16QAM-3/4	3
5	64QAM-1/2	3
6	64QAM-2/3	4
7	64QAM-3/4	4.5
8	64QAM-5/6	5

Table 3.5: Modulation and coding schemes.

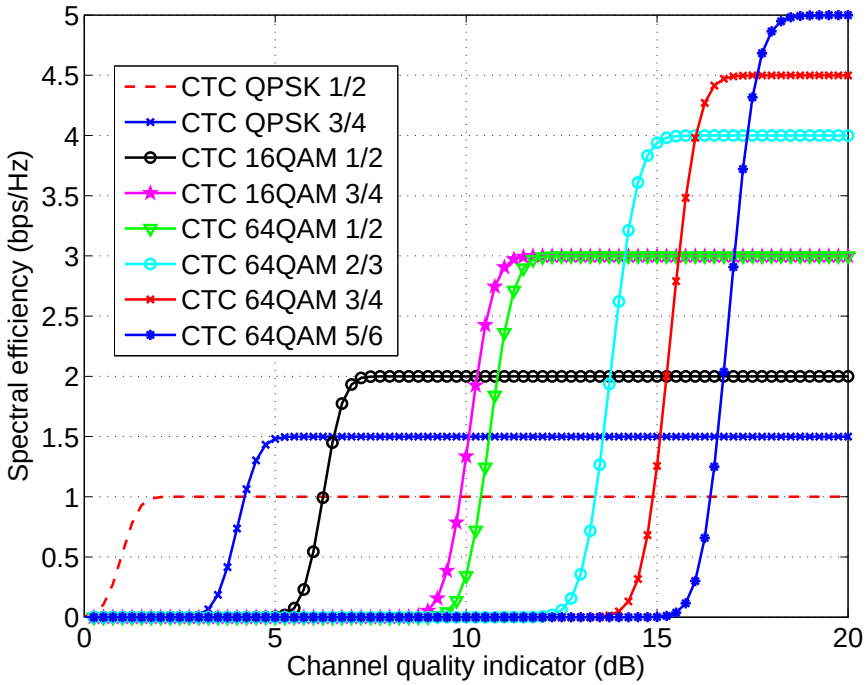

Figure 3.9: Spectral efficiency vs. SNR for CTC.

where $MCS_{u,r}$ is the chosen MCS of the u^{th} MS for the r^{th} RB and $CQI_{u,r}$ is the CQI sent by the u^{th} MS for the r^{th} RB. If there is no MCS that supports target BLER, we select the lowest MCS, namely QPSK-1/2. Target BLER is specified in Table 3.3. We should note that reliability of CQI information effects the performance of the AMC algorithm directly.

Scheduling subblock : In the simulations, scheduling is done at the beginning of each frame. Scheduler gives the highest priority to HARQ retransmissions. The packets that need to be retransmitted are allocated to RBs with first priority.

After the packets that need to be retransmitted are assigned to RBs, the remaining RBs are allocated with the scheduling methods explained below.

Proportional fair (PF) scheduling : PF algorithm schedules the user whose ratio of instantaneous achievable rate to average rate is maximum. In [6], the PF algorithm, described in [19], is extended for OFDMA systems. Scheduled user, u^*, on the p^{th} RB is determined as

$$u^* = \arg \max_{u:1 \leq u \leq N_{sec}} \frac{R_{u,p}[t]}{r_u}, \tag{3.18}$$

where N_{sec} is the number of MSs per sector, t is the scheduling instant. $R_{u,p}[t]$ is the instantaneous achievable rate of user u on the p^{th} RB at time t and is the function of a CQI feedback, which can be expressed as

$$R_{u,p}[t] = \log_2(CQI_{u,p}[t]), \tag{3.19}$$

where $CQI_{u,r}$ is the CQI sent by the u^{th} MS for the r^{th} RB. In Eq. 3.18, r_u is the moving average of the instantaneous rates of user u. Metric r_u is updated after scheduling each RB. The update is as follows,

$$r_u = \begin{cases} \alpha R_{u,p}[t] + (1-\alpha) r_u, & u = u^* \\ (1-\alpha) r_u, & u \neq u^* \end{cases} \tag{3.20}$$

where α is the coefficient of the low pass filter used to average the instantaneous rates. $\alpha = \dfrac{T_{frame}}{P \times T_{PF}}$ where T_{frame} is the duration of a WiMAX frame, P is the number of RBs and T_{PF} is the latency time.

Maximum sum rate (MSR) algorithm : MSR algorithm schedules the user who has the best channel condition. Scheduled user, u^*, on the p^{th} RB is

determined as

$$u^* = \arg \max_{u:1 \leq u \leq N_{sec}} R_{u,p}[t]. \quad (3.21)$$

Round robin (RR) algorithm : In RR algorithm, each user is scheduled one by one. A user will not be re-scheduled before the other users are scheduled.

Channel pass subblock : Interfering channels for each MS are generated with the duration of the DL subframe. We assume that MSs do not interfere with each other and only sectors interfere with MSs. We separate the interferers into strong and weak interferers according to the link gains. I_{strong} strongest interferes are named as strong interferers and the remaining ones as weak interferers. I_{strong} value is specified in Table 3.3. Channel for strong interferers includes the effect of fast and slow fading. For weak interferers, we do not model the fast fading. This process reduces the computational complexity.

Post-processing SINR computation subblock : Post-processing SINR values are computed for each data subcarrier located in the data regions of WiMAX DL subframe. In the simulations, we assume that each MS tracks the DL channel with its serving sector and interfering sectors perfectly. Due to this assumption, in the simulations, we do not use the functionality of the pilot subcarriers.

CQI feedback subblock : CQI is reported for each RB. Computation of a CQI for a RB is carried out by computing the SINR values experienced on the subcarriers which are located in the initial OFDM symbol of that RB, and then compressing into an value as in Eq. 3.13.

In real systems, CQI may be received erroneously at BS. However, we assume in our simulations that CQI feedback channel does not introduce any error.

CQI feedback reaches BS within a certain time delay. This delay has an important role in the performance of system especially in fast varying channels. In our simulations, CQI feedback delay is equal to 15 ms.

PER estimation subblock : PER is estimated as shown in Eq. 3.15. We flip a coin with probability PER to determine whether the packet is received successfully or unsuccessfully. If the received packet is in error after the maximum number of retransmissions, the packet is discarded. If the received packet is in error and the maximum number of retransmissions is not exceeded, the packet is retransmitted. However, the packet is not retransmitted immediately. It becomes ready to be retransmitted after a certain retransmission delay. Parameter values describing the minimum retransmission delay and the maximum number of retransmissions are specified in Table 3.3.

3.4.3.3 Metric Computation

At the end of each drop, we calculate the performance metrics for each MS and sector on the central cluster and store them to use at the "Performance Analysis" part. Performance metrics are user data throughput, sector data throughput, user average packet retransmission, and spectral efficiency. Descriptions of the metrics are as follows.

User data throughput is the ratio of the number of successfully received information bits to the simulation time for the MS of interest. User data throughput is computed as

$$T^{(u)} = \frac{\sum_{p=1}^{N_{packet}^{(u)}} B_{u,p}}{T_{sim}}, \quad \text{(bps)} \tag{3.22}$$

where $T^{(u)}$ is the data throughput of MS u, $N_{packet}^{(u)}$ is the number of successfully received packets for the u^{th} MS, $B_{u,p}$ is the number of information bits at the p^{th} successfully received packet for the u^{th} MS, and T_{sim} is the simulation time.

Sector data throughput is the sum of the data throughput of the MSs that are served by the sector of interest and computed as

$$S^{(s)} = \sum_{i=1}^{N_{sec}} T^{(u_i)}, \quad \text{(bps)} \tag{3.23}$$

where S^s is the data throughput for the s^{th} sector and $\{u_1, u_2, \cdots, u_{N_{sec}}\}$ are the indexes of the MSs served by sector s.

Spectral efficiency is computed once the sector throughputs of each sector are computed. Spectral efficiency is computed as

$$SE = \frac{S}{BW \times TD}, \tag{3.24}$$

where S is the average sector throughput, BW is the bandwidth assigned to each sector and TD is the ratio of the DL subframe duration to the frame duration.

User average packet retransmission is the average retransmission of the packets successfully received by the MS of interest and computed as

$$T^{(u)} = \frac{\sum_{p=1}^{N^u_{packet}} r_{u,p}}{N^u_{packet}}, \tag{3.25}$$

where $T^{(u)}$ is the average packet retransmission for MS u and $r_{u,p}$ is the number of the retransmission of the p^{th} successfully received packet for the u^{th} MS.

In addition to the metrics given above, the distribution of the selected MCSs for each MS and the distance of MSs to their serving sectors are stored.

3.4.4 Analysis

In the analysis part, performance metrics that we store at each drop are loaded and combined. We have performance informations of M_{user} MSs and M_{sector} sectors where

$$M_{user} = N_{drop} \times C \times N_{sec}, \tag{3.26}$$

$$M_{sector} = N_{drop} \times C. \tag{3.27}$$

C is the number of sectors per cluster and given in Table 3.3. Based on these informations, cumulative distributions of the user average throughput sector throughput, and user average packet retransmission are plotted. Figures including the distribution of MCSs are also plotted.

Chapter 4

Simulations and Results

In this chapter, we present our simulation results. In the simulations, simulation time is 1.5 seconds and drop number is equal to 5. We analyze 300 frames per drop. Default values, given in Table 4, are used for the input parameters unless otherwise stated.

Parameter	**Value**
Traffic	Full buffer
Scheduling method	PF
Coding scheme	CTC
PHY abstraction method	EESM
Number of RBs per frame	5
Antenna configuration	SISO
Subchannelization	PUSC
Number of MSs per sector N_{sec}	10
Speed	mix
Frequency reuse pattern	1x3x1

Table 4.1: Default values of the input parameters used in the simulations.

4.1 Frequency Reuse Model

Section 3.2 specifies the frequency reuse models, 1x3x1, 1x3x3, 3x3x1, we have used in the simulations. Figure 4.1 displays the sector throughput of these reuse patterns. We observe that the throughput performance of 1x3x1 reuse pattern is

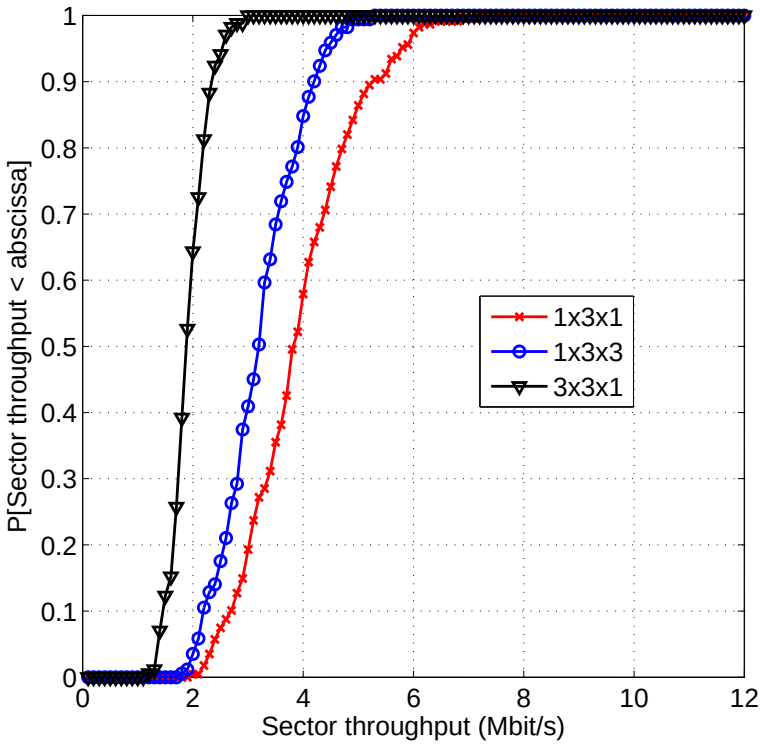

Figure 4.1: CDFs of the sector throughputs for 1x3x1, 1x3x3, and 3x3x1 reuse models.

better than the other two reuse patterns' throughput performance. The reason is as follows. In 1x3x1 reuse pattern, each sector is assigned the entire bandwidth but in 1x3x3 and 3x3x1 reuse patterns, each sector is assigned one third of the entire bandwidth. From Figure 4.1, we can see that the performance of 3x3x1 reuse mode is worse than the performance of 1x3x3 reuse mode. Since each sector within the cell is assigned the same spectrum band, inter sector interference within the cell limits the performance of 3x3x1 reuse mode.

In 1x3x1 reuse mode, there are maximum number of interferers for the given sector because each sector is assigned the same spectrum band. Therefore, the

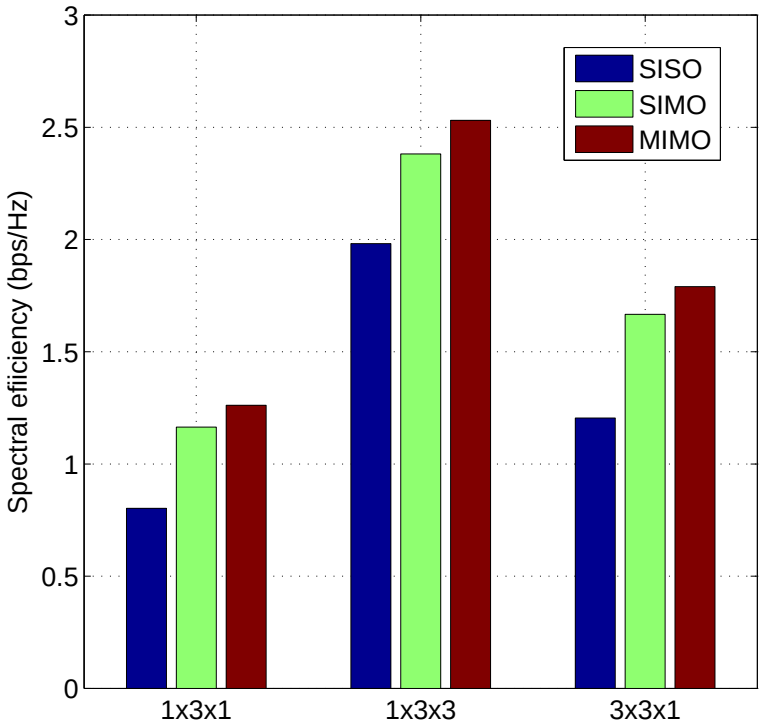

Figure 4.2: Spectral efficiencies of 1x3x1, 1x3x3, and 3x3x1 frequency reuse models for SISO, SIMO, and MIMO antenna configurations.

worst received signal quality can be found on 1x3x1 reuse mode. From Figure 4.2, we can observe that 1x3x1 reuse mode has the worst spectral efficiency for all antenna configurations. Maximum spectral efficiency, 2.53 bps/Hz, appears in MIMO-1x3x3 configuration.

4.2 Mobility

We compare the coherence time of channel and the CQI feedback delay to analyze the effect of mobility. In the simulations, the CQI feedback delay is 15 ms as specified in Table 3.3. In [20, Chapter 4], coherence time (T_c) is calculated as

$$T_c = \frac{0.423}{f_d} \quad \text{(sec)}, \tag{4.1}$$

where f_d is the maximum Doppler shift in Hz.

- When the speed of MS is 3 km/h, the coherence time is 62.35 ms. Since the coherence time is larger than the CQI feedback delay, we can observe that CQI feedback reflects the current state of channel accurately.

- When the speeds of MS are 30 km/h and 120 km/h, coherence times are 6.23 ms and 1.56 ms respectively. Coherence times are smaller than the CQI feedback delay; therefore, CQI feedbacks are not reliable on the current frame. Selected MCSs do not match with channel conditions because of the inaccurate CQI feedbacks.

At high speeds, the selected MCSs for current packets do not match with the current channel conditions. Therefore, packets are retransmitted more frequently. Figure 4.3 shows the average user packet retransmission at different speeds. Since resources are wasted with the packet retransmissions, user and sector throughputs decrease at higher speeds as seen in Figures 4.4-4.5.

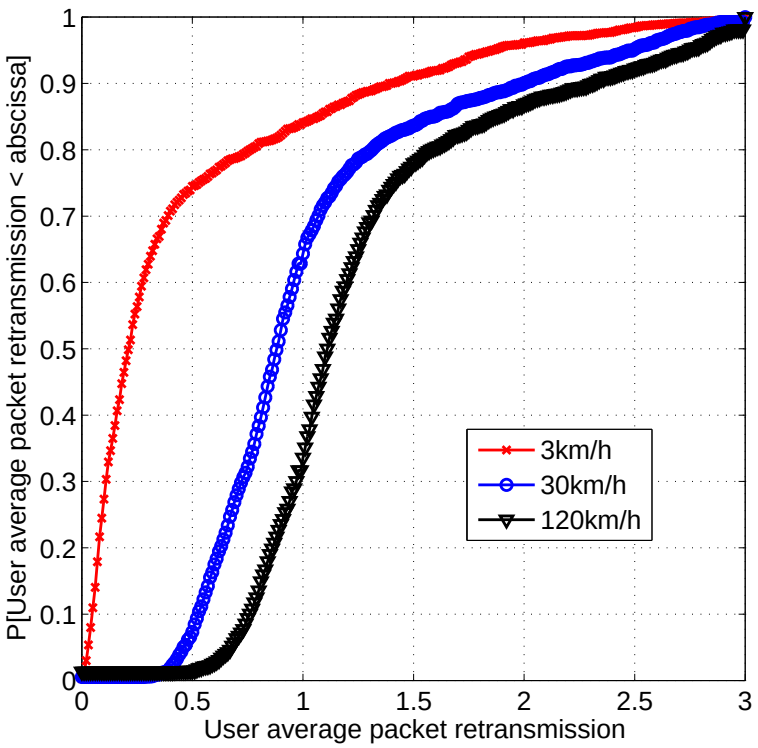

Figure 4.3: CDFs of the user average packet transmissions at 3 km/h, 30 km/h, and 120 km/h velocities.

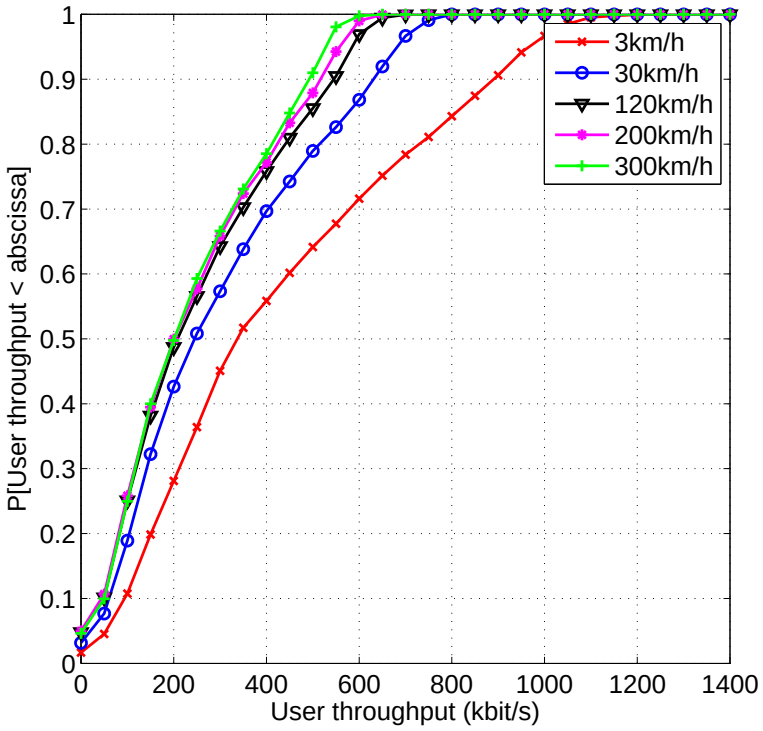

Figure 4.4: CDFs of the user throughputs at 3 km/h, 30 km/h, 120 km/h, 200 km/h, and 300 km/h velocities.

From Figures 4.4-4.5, we can observe that the throughput gap between 30 km/h and higher speeds is much lower than the throughput gap between 3 km/h and 30 km/h. In the simulations, MSs are fixed; therefore, path loss and shadowing effect do not change over time. Since coherence time for high speeds (120 km/h, 200 km/h, 300 km/h) is lower than the CQI feedback delay, the curves plotted for high speeds are close to each other.

4.3 Subchannelization

Band AMC is employed to exploit the multiuser diversity in frequency selective channels. To reflect the frequency selectivity of channels, each RB should span a bandwidth that is smaller than the coherence bandwidth. In [20, Chapter 4], coherence bandwidth (B_c) is calculated as

$$B_c = \frac{1}{5\sigma}, \quad \text{(Hz)} \tag{4.2}$$

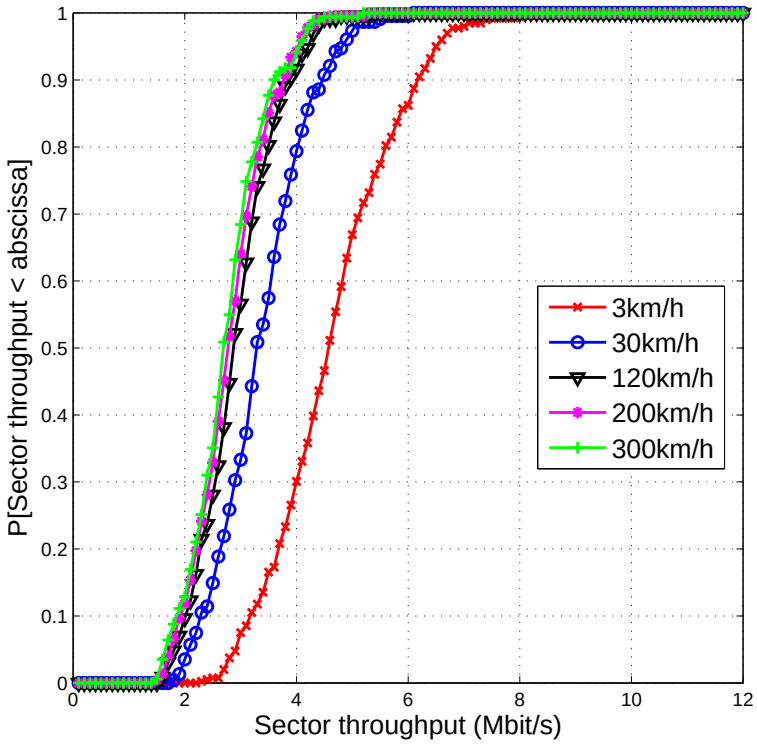

Figure 4.5: CDFs of the sector throughputs at 3 km/h, 30 km/h, 120 km/h, 200 km/h, and 300 km/h velocities.

where σ is the maximum delay spread of channel in seconds. The coherence bandwidths of ITU modified pedestrian B and vehicular A channels are 312.69 kHz and 564.65 kHz respectively. We assign a single subchannel to each RB in band AMC subchannelization so each RB spans 262.65 kHz. In 1x3x1 frequency reuse pattern, this configuration corresponds to 30 RBs per frame. Figure 4.6 shows the effect of RB number per frame on the system performance. In the scenario which there is 5 RBs per frame, user diversity is totally lost.

In band AMC subchannelization, subcarriers at each symbol experience highly correlated fast fading. In PUSC, subcarriers at each symbol experience uncorrelated fast fading. Therefore, we can conclude that CQI[1] for a RB varies faster in band AMC mode through time. In time-selective channels with a coherence time smaller than the CQI feedback delay, PUSC is employed to maximize the system performance. Figure 4.7 shows the effect of mobility on PUSC and

[1]Calculation of CQI can be seen in Section 3.4.3.

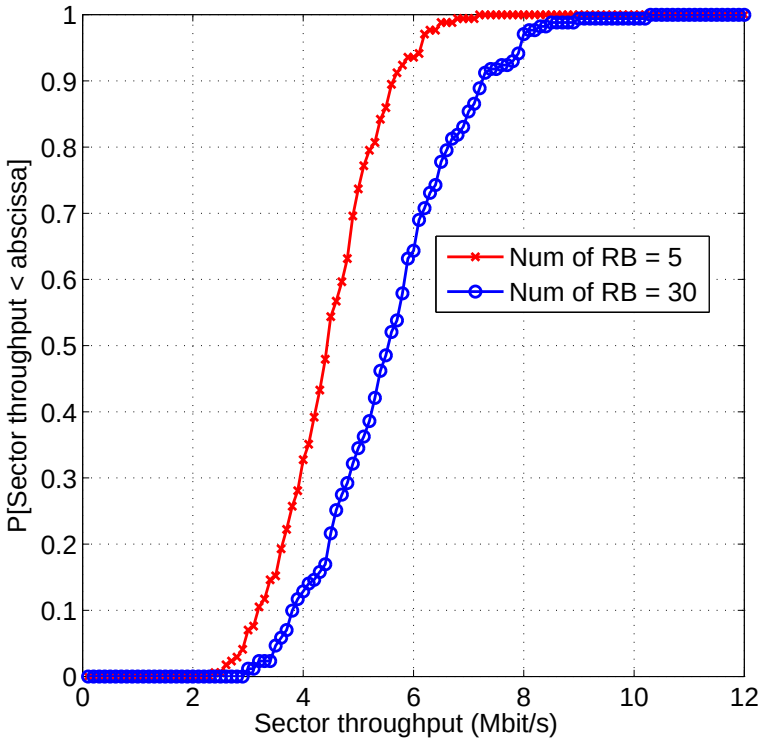

Figure 4.6: CDFs of the sector throughputs for 5 and 10 resource blocks per frame at 3 km/h velocity.

band AMC subchannelization. It can be observed that band AMC outperforms PUSC in low mobility cases with the help of user diversity. However, user diversity can not be exploited at high mobility cases because of the unreliable CQI feedbacks. PUSC outperforms band AMC at high mobility.

4.4 Scheduling

Up to this point, we have used PF scheduling in the simulations. Figure 4.8 shows the distribution of sector throughputs for the scheduling algorithms described in Section 3.4.3.

From Figure 4.8, we can observe that MSR algorithm outperforms the other two algorithms. The reason is as follows. In MSR algorithm, a RB is allocated to the MS who has the best channel condition on that RB. Therefore,

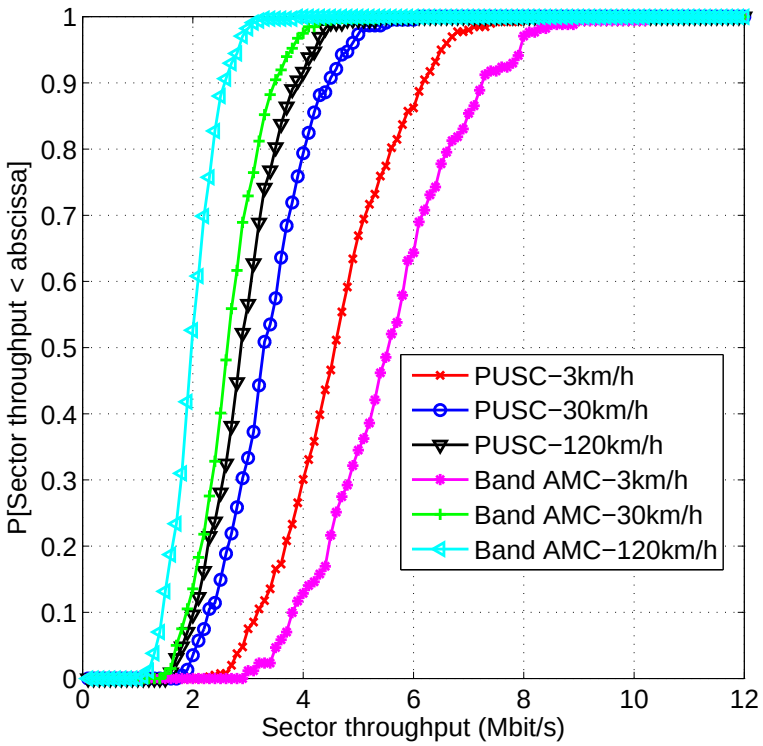

Figure 4.7: CDFs of the sector throughputs for PUSC and band AMC subchannelization methods at 3 km/h, 30 km/h, and 120 km/h velocities.

MSR algorithm maximizes the sector throughput. RR algorithm has the worst performance because it is unaware of the channel conditions of MSs.

From Figure 4.9, it can be observed that MSR algorithm does not support the MSs who are far from the serving BS. We can conclude that MSR algorithm is not a fair algorithm.

In Figure 4.10, we analyze the performance of scheduling algorithms for different number of MSs per sector. Simulations are done in 3 km/h velocity and band AMC subchannelization. We drop 10, 15, 20, 25 and 30 MSs per sector for each scheduling method.

From Figure 4.10, we can observe that the performance of RR algorithm is nearly the same for different number of MSs per sector. The reason is that CQI feedbacks are not used in RR algorithm; therefore, multiuser diversity is not

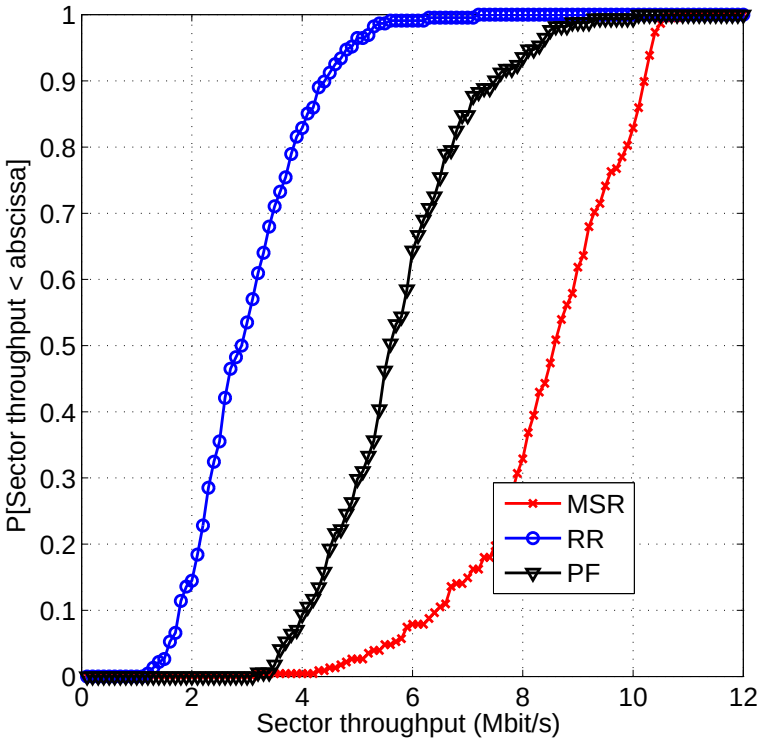

Figure 4.8: CDFs of the sector throughputs for MSR, PF, and RR scheduling methods.

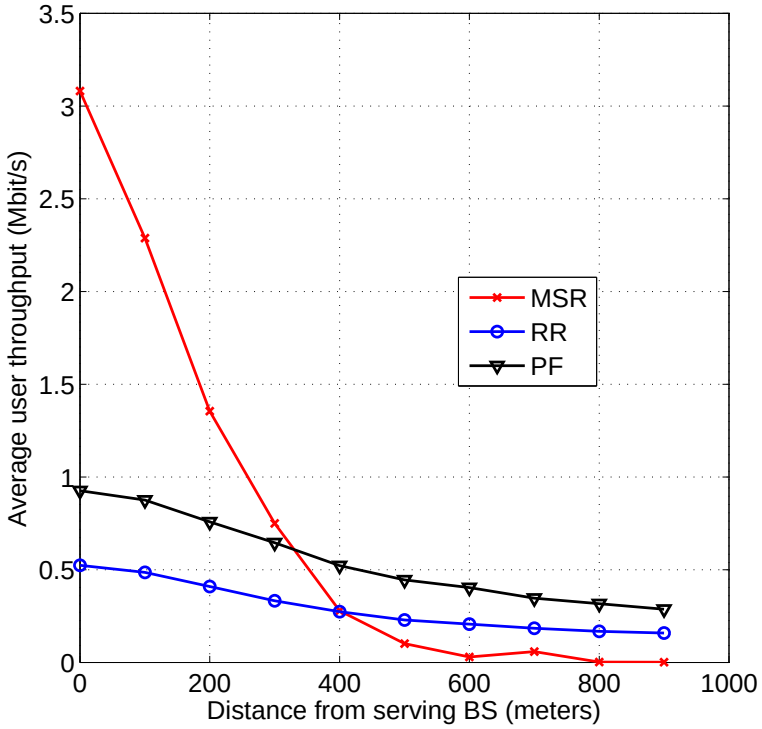

Figure 4.9: Average user throughput vs. distance from serving BS for MSR, PF, and RR scheduling methods.

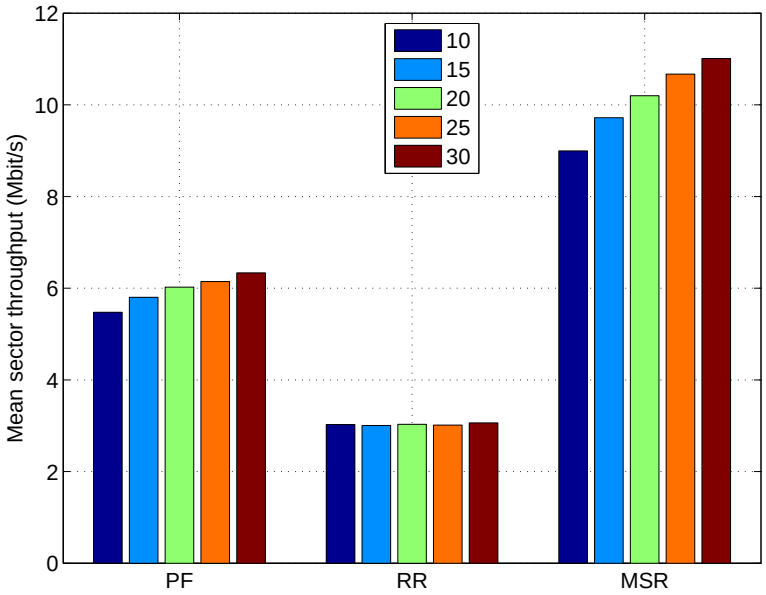

Figure 4.10: Mean sector throughputs for PF, RR, and MSR scheduling methods each of which is analyzed at 10, 15, 20, 25, and 30 MSs per sector

exploited in this algorithm. Moreover, multiuser diversity is exploited best in MSR algorithm because this algorithm does not give a fair service to MSs.

4.5 Comparative Analysis of Polar Code and CTC

BLER vs SNR curves for the profiles 9, 15, 20, 26, 28, 30, and 32 in Table 2.6 are shown in Figure 4.11. The AMC algorithm explained in Section 3.4.3 selects MCS according to the received CQI feedback. From 4.11, we can observe that in the same channel conditions, the AMC algorithm using polar code selects low order MCSs more frequently than the AMC algorithm using CTC. This is clearly apparent in Figure 4.12 that shows percentage of selected MCSs for CTC and polar coding. We can see that in polar code configuration, high order MCSs are not supported even in the low distances to BS. Therefore, we except throughput degradation in polar code scenario. Figures 4.13-4.15 display the comparison of polar code and CTC.

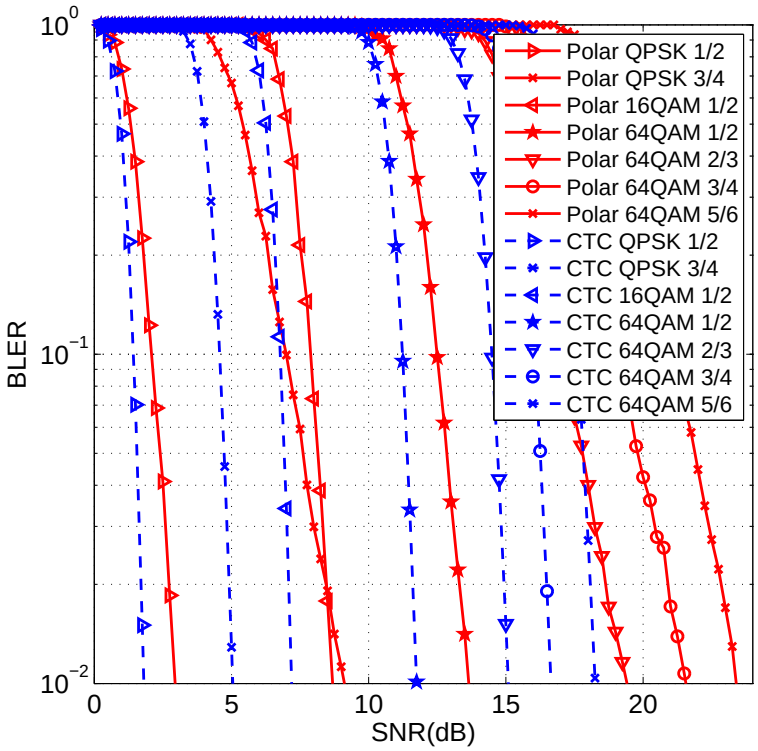

Figure 4.11: BLER vs. SNR for polar code and CTC under AWGN channel

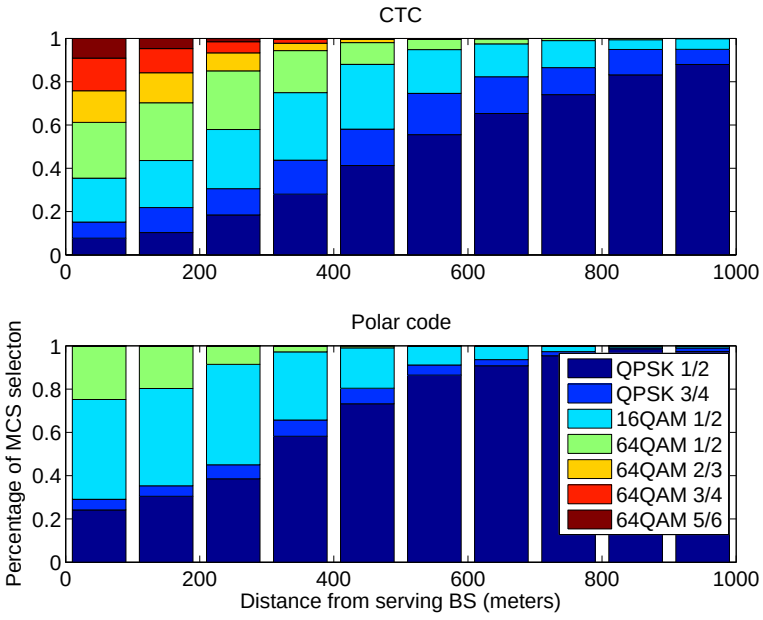

Figure 4.12: Percentage of selected MCSs vs. distance from serving BS for polar code and CTC.

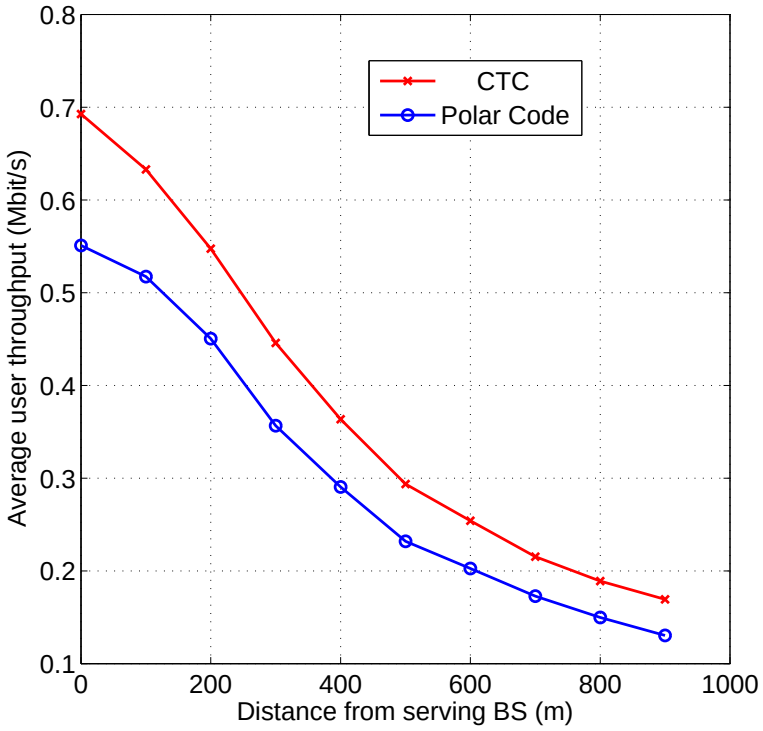

Figure 4.13: Average user throughput vs. distance from serving BS for polar code and CTC.

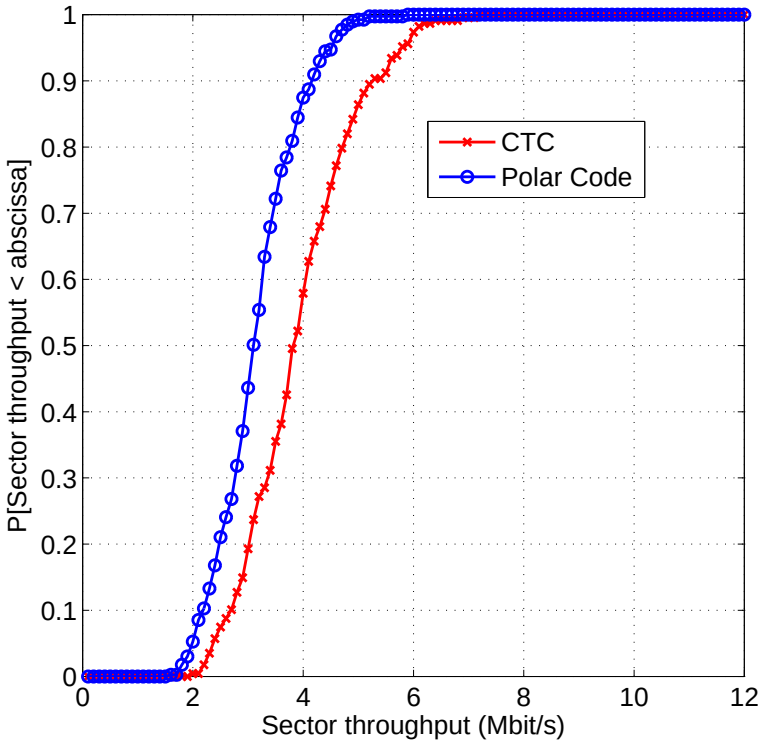

Figure 4.14: CDFs of the sector throughputs for polar code and CTC.

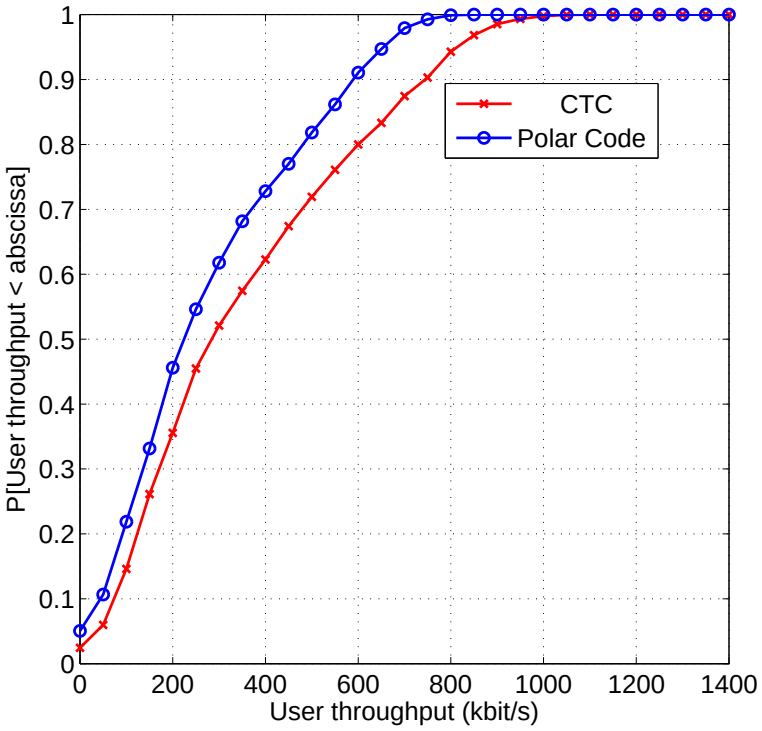

Figure 4.15: CDFs of the user throughputs for polar code and CTC.

Chapter 5

Conclusion

5.1 Summary

In this thesis work, we have implemented a WiMAX system level simulator in MATLAB based on the methodology provided in Chapter 4. In the system level simulations, we have analyzed the system level performance of algorithms and frequency reuse patterns that are described in Chapter 4. Finally, we have done a comparative analysis of polar code and CTC on WiMAX network.

We have observed that CQIs vary faster through time in band AMC subchannelization. Therefore, PUSC is preferred in high mobility. In low mobility cases, band AMC outperforms PUSC because of the user diversity.

Maximum spectral efficiency is obtained in 1x3x3 frequency reuse pattern because sectors using the same spectrum band are isolated best from each other in this reuse pattern. In 1x3x1 frequency reuse pattern, we can observe the maximum throughput because each sector is assigned the entire bandwidth.

We have observed that RR algorithm has the worst performance and user diversity is not exploited in this algorithm. In MSR algorithm, cell edge users are not scheduled.

The system level performance of CTC is better than the system level performance of polar code. This is an expected result because CTC outperforms polar code in the link level simulations done for each MCS under AWGN channel.

5.2 Future Work

In the simulations, we have considered only DL transmission. UL simulation can be considered as a future work. Puncturing of polar code is an open research area. New techniques can be proposed that have better performance than the puncturing method explained in Appendix A.

APPENDIX A

Polar Codes

Polar coding achieves the symmetric capacity of binary-input discrete memoryless channels [12] and the symmetric capacity is equal to the channel capacity when the channel is symmetric. We will skip the theoretical analysis of polar coding which is explained in [12]. We will only explain how polar codes are implemented in the link level simulations.

For (N, K) polar code, $K \times N$ generator matrix $G_P(N, K)$ is a submatrix of $F^{\otimes n}$ for any $n \geq 1$, $N = 2^n$, and $K < N$ where $F = \left[\begin{smallmatrix} 1 & 0 \\ 1 & 1 \end{smallmatrix}\right]$ and $F^{\otimes n}$ is the n^{th} Kronecker power of matrix F.

K rows of $F^{\otimes n}$ are selected to generate $G_P(N, K)$. $z_n = (z_{N,1} \ldots, z_{N,N})$ vector is generated for selection. The recursive computation of the z_n vector is as follows [21]:

$$z_{2k,j} = \begin{cases} 2z_{k,j} & \text{for } 1 \leq j \leq k \\ z_{k,j} & \text{for } k+1 \leq j \leq 2k \end{cases} \tag{A.1}$$

The recursive computation begins with $z_{1,1} = 0.5$. According to the vector $z_n = (z_{N,1} \ldots, z_{N,N})$, permutation vector $\pi = (i_1, \ldots, i_N)$ is created from the set $(1, \ldots, N)$ such that $z_{n,i_j} \leq z_{n,i_k}$, and $j \leq k$. Generator matrix $G_P(N, K)$ is composed of the rows of $F^{\otimes n}$ with indexes $i_1, \ldots, i_K$.

We make a comparative analysis of polar code and CTC in the system level simulations. To make a fair comparison, polar codes should have the same block lengths with CTC. Table 2.6 specifies the block lengths of CTC used in the system level simulations.

The recursive construction of polar codes allows only code lengths of 2^n for any $n \geq 1$. Therefore, we have to puncture polar codes to have the same block lengths with CTC. The puncturing method we are using in the link level simulations is as follows. For any (N, K) code profile given in Table 2.6, we firstly find the smallest $N^{'}$ such that $N \leq N^{'}$, and $N^{'} = 2^n$ for any $n \geq 1$. According to the code construction method given in Eq. A.1, we construct $(K, N^{'})$ polar code. $(N^{'} - N)$ bits are randomly selected from the coded bits with indexes $(i_{K+1}, \ldots, i_{N'})$ and are deleted to generate (K, N) polar code.

Successive cancellation (SC) decoding algorithm [12] is used in the link level simulations. Bit log-likelihood ratios (LLR) are computed for each received bit and SC decoding algorithm takes LLR values as input. In the case of puncturing, LLR values of punctured bits are set to zero.

Bibliography

[1] S. Ahmadi, "An Overview of Next-Generation Mobile WiMAX Technology," *IEEE Communications Magazine*, vol. 47, no. 6, pp. 84–98, June 2009.

[2] "IEEE Standard for Local and Metropolitan Area Networks–Part 16: Air Interface for Fixed and Mobile Broadband Wireless Access Systems," February 2006. [Online]. Available: http://standards.ieee.org/getieee802/download/802.16e-2005.pdf

[3] B. Li, Y. Qin, C. P. Low, and C. L. Gwee, "A Survey on Mobile WiMAX," *IEEE Communications Magazine*, vol. 45, no. 12, pp. 70–75, Dec. 2007.

[4] J. G. Andrews, A. Ghosh, and R. Muhamed, *Fundamentals of WiMAX: Understanding Broadband Wireless Networking*, ser. Prentice Hall Communications Engineering and Emerging Technologies Series, S. Rappaport, Ed. Prentice Hall, February 2007.

[5] L. Xiaojia, J. Antikainen, V. Tapio, J. Ylitalo, R. Parviainen, A. Harkonen, and M. Juntti, "Link Level Simulation Study of Downlink MIMO and Uplink HARQ in IEEE 802.16e WiMAX System," in *Proc. IEEE 69th Vehicular Technology Conference (VTC2009-Spring)*, Barcelona, Spain, April 2009, pp. 1–5.

[6] "802.16m Evaluation Methodology Document," January 2009. [Online]. Available: http://www.ieee802.org/16/tgm/docs/80216m-08_004r2.pdf

[7] R. Srinivasan, S. Timiri, A. Davydov, and A. Papathanassiou, "Downlink Spectral Efficiency of WiMAX," in *Proc. IEEE 65th Vehicular Technology Conference (VTC2007-Spring)*, Dublin, Ireland, April 2007, pp. 2786–2790.

[8] T. Chunchang, J. Jing, and X. Zhang, "Evaluation of Mobile WiMAX System Performance," in *Proc. IEEE 68th Vehicular Technology Conference (VTC2008-Fall)*, Calgary, Canada, Sep. 2008, pp. 1–5.

[9] C. F. Ball, E. Humburg, K. Ivanov, and F. Treml, "Performance Evaluation of IEEE 802.16 WiMAX with Fixed and Mobile Subscribers in Tight Reuse," *European Transactions on Telecommunications*, pp. 203–218, March 2006.

[10] "Mobile WiMAX Part II: A Comparative Analysis," May 2006. [Online]. Available: http://www.wimaxforum.org/technology/downloads/Mobile_WiMAX_Part2_Comparative_Analysis.pdf

[11] Y. Gao, X. Zhang, D. Yang, and Y. Jiang, "Unified Simulation Evaluation for Mobile Broadband Technologies," *IEEE Communications Magazine*, vol. 47, pp. 142–149, 2009.

[12] E. Arıkan, "Channel Polarization: A Method for Constructing Capacity-Achieving Codes for Symmetric Binary-Input Memoryless Channels ," *IEEE Transactions on Information Theory*, vol. 55, no. 8, pp. 3051–3073, 2009.

[13] "IEEE Standard for Local and Metropolitan Area Networks–Part 16: Air Interface for Fixed and Mobile Broadband Wireless Access Systems," May 2009. [Online]. Available: http://standards.ieee.org/getieee802/download/802.16-2009.pdf

[14] Z. Tao, A. Li, J. Zhang, and T. Kuze, "Performance Improvement for Multichannel HARQ Protocol in Next Generation WiMAX System," in *Proc. IEEE Wireless Communications and Networking Conference (WCNC 2008)*, Las Vegas, Nevada, USA, March 2008, pp. 2009–2014.

[15] A. Goldsmith, *Wireless Communications*. Cambridge: Cambridge University Press, 2005.

[16] S. Tiraspolsky, A. Rubtsov, A. Maltsev, and A. Davydov, "Mobile WiMAX - Deployment Scenarios Performance Analysis," in *Proc. Third International Symposium on Wireless Communications Systems (ISWCS'06)*, Valencia, Spain, Sep. 2006, pp. 353 – 357.

[17] "WiMAX System Evaluation Methodology, Version 2.1." [Online]. Available: http://www.cse.wustl.edu/~jain/wimax/ftp/wimax_system_evaluation_methodology_v2_1.pdf

[18] S. M. Alamouti, "A Simple Transmit Diversity Technique for Wireless Communications," *IEEE Journal on Selected Areas in Communications*, vol. 16, no. 8, pp. 1451–1458, 1998.

[19] A. Jalali, R. Padovani, and R. Pankaj, "Data Throughput of CDMA-HDR a High Efficiency-High Data Rate Communication Wireless System," in *Proc. IEEE 51st Vehicular Technology Conference (VTC2000-Spring)*, vol. 3, Tokyo, 2000, pp. 1854–1858.

[20] T. S. Rappaport, *Wireless Communications: Principles and Practice, 2nd ed.*, ser. Prentice Hall Communications Engineering and Emerging Technologies Series, T. S. Rappaport, Ed. Prentice Hall, 2002.

[21] E. Arıkan, "A Performance Comparison of Polar Codes and Reed-Muller Codes," *IEEE Communication Letters*, vol. 12, no. 6, pp. 447–449, June 2008.